Plasma Diagnostics in Negative Ion Sources by Laser Photodetachment

Masaki Nishiura

DOCTOR OF SCIENCE

Department of Fusion Science
School of Mathematical and Physical Science
The Graduate University for Advanced Studies

1998

Abstract

Various phenomena due to negative ions in plasmas are widely studied by many researchers in astrophysics, atomic physics, chemistry, and plasma physics. These fields sometimes involve curious phenomena that can not be explained without any consideration of the inherent properties of negative ions. Hence, negative ion diagnostics are essential to understanding of behavior of negative ions and interactions among plasma particles. The photodetachment technique becomes a powerful diagnostic tool for determination of negative ion densities and its temperatures in plasmas.

In the first part of this thesis, studies on plasma responses after a photodetachment reaction have been carried out both theoretically and experimentally. In the second half, the diagnostic techniques for negative ion densities and temperatures measurement are applied to an actual H^- ion source. In particular when cesium vapor is introduced into a hydrogen discharge, an anomalous enhancement of H^- is observed. The combination with photoelectron current measurements on a plasma electrode and the other plasma parameter measurements, including the measurements of negative ion densities, allows us to discuss the enhancement mechanism of H^- in a cesium seeded case.

First stage of the study on the laser photodetachment technique is the investigation of the influence of the energies of photodetached electrons upon the determination of the H^- density and the H^- drift velocity in a hydrogen plasma by using the fundamental frequency (1064 nm), the 2nd harmonic (532 nm) and the 3rd harmonic (355 nm) of a Nd-YAG laser. It is found that the $\delta I_p - V_p$ characteristics, where δI_p is the photodetachment current and V_p is the probe voltage, do not depend on the photon energies. The effective temperature of photodetached electrons T_{eff} is close, within 40 %, to that of background electrons. As a result the measurements of the H^- density and the H^- drift velocity are not affected by photon energies.

Next, the entire dynamics and physical picture of plasma response after laser photodetachment have been studied theoretically and experimentally. The hybrid fluid-kinetic model of Friedland et al., where negative ions are treated in a ballistic approximation, electrons in a linearlized Boltzmann's relation, and positive ions as a fluid, is extended to the analysis of perturbed densities inside and outside a laser beam. From the results of calculations, the time evolution of perturbed electron current is in good agreement with experimental data. The overshoot in the perturbed electron current, which is frequently seen under some experimental conditions, has been studied. From the comparison of overshoot signals between the observation and the calculation, the way of the determination of positive ion temperature is proposed.

The rest in this thesis concentrates on the cesium effect of negative ion densities both in driver region and in extraction region of an ion source of volume production type, because it has been reported that beam intensity of negative ions from a negative ion source is enhanced drastically after a cesium injection into an H^- ion source. In a cesium seeded hydrogen discharge, the H^- density and temperature by use of the laser photodetachment technique are investigated in the driver region of tandem H^- source, in which the plasma is not connected directly with the wall of the ion source. The amount of cesium in the ion source is monitored by spectroscopic

measurement. The plasma space potential, V_s, obtained from the probe $I-V$ characteristics has increased by Cs injection. However no clear changes in n_e, n_-, T_e, T_+, and T_- are observed. This result suggests that the wall surface in the extraction region influence the H^- production in the Cs/H_2 discharge.

For the purpose of studies on the cesium effect in an extraction region of an ion source, the work function of the plasma electrode surface is measured photoelectrically using an Ar^+ ion cw laser. The mount of alkali metal vapor is measured by spectroscopic method, and negative ion densities are measured by photodetachment method. The measured work function is correlated with the H^- density measured simultaneously by the laser photodetachment technique. As the work function of the plasma electrode is reduced due to Cs seeding, the ratio of H^- density to electron density, n_-/n_e, increased gradually. The n_-/n_e ratio becomes maximum when the work function reaches at the minimum value. The same result is obtained in the case of Rb seeding. These results are discussed with the help of rate equations in the plasma, taking the surface effects into account.

This work can be summarized as the following; H^- ions and other plasma species in negative ion sources can be diagnosed by means of the laser photodetachment technique. From the agreement between the theoretical calculations and experimental results, it is found that the hybrid-fluid kinetic model is valid under the conditions of the collisionless, unmagnetized and low n_-/n_e ratio, described here, and that it is useful to determine the H^- density, H^- temperature, and positive ion temperature. It is confirmed that the work function of the surface of the plasma electrode of a cesium seeded H^- volume source influences the n_-/n_e ratio in the extraction region.

Contents

Part I

Basis for ion source diagnostics, photodetachment theory and experiment

Chapter 1

Introduction

1.1 Production of negative ions

Negative ions [1, 2] occasionally exist in a cold plasma. In general, the energy to detach an electron from a negative ion, that is called electron affinity, can be calculated using the quantum theory. The electron affinity of an element determines whether the negative ion can exist in a stable state or not. For example, the electron affinity of hydrogen is 0.754 eV. In addition to these ground state negative ions, when an extra electron is bound relative to the excited metastable state of the neutral, some negative ions(He^-, Be^-, Mg^-, and etc.) exist in stable states. Molecular negative ions exist as well. In this thesis we deal mainly with H^- ions in an ion source.

Formation of negative ion by volume production

In a gas discharge plasma, various collisional processes with electrons, atoms, and molecules can be considered. In these processes, dissociative attachment of electrons was considered to be most possible reaction for the production of negative ions of hydrogen isotopes;

$$e + AB \rightarrow A^- + B.$$

However the cross section for this reaction was thought to be very small. Schulz et al. [3] measured the total negative ion production in H_2 as a function of electron energy in 1959. After a few years, Rapp et al. [4] obtained the cross sections for negative ion production in H_2, HD, and D_2. Two resonant peaks of cross sections suggest the existence of quantum levels, corresponding to vibrational and rotational states, respectively. Schulz and Asundi also measured the cross sections for dissociative attachment of electrons, as well as the isotope effect, in the lower electron energy region than those of Rapp's results.

According to the energy diagram of H_2^-, H_2, and H_2^+, as shown in Fig. 1.1, the energy potential curves for $^2\Sigma_g^+$ and $^2\Sigma_u^+$ states of H_2^- lie above the potential curve for the ground $^1\Sigma_g^+$ state of H_2, when the internuclear separation is less than 1.8 Å. As increasing the nuclear separation more than 1.8 Å, we can see the inversion of states between $H_2(X^1\Sigma_g^+)$ and $H_2^-(^2\Sigma_{u,g}^+)$. If H_2 molecules are excited to a higher energy level than that of H + H^-, H_2 molecules would dissociate to H + H^-, and thus H^- ions are produced. This reaction is called the dissociative attachment of electrons to vibrationally excited molecules.

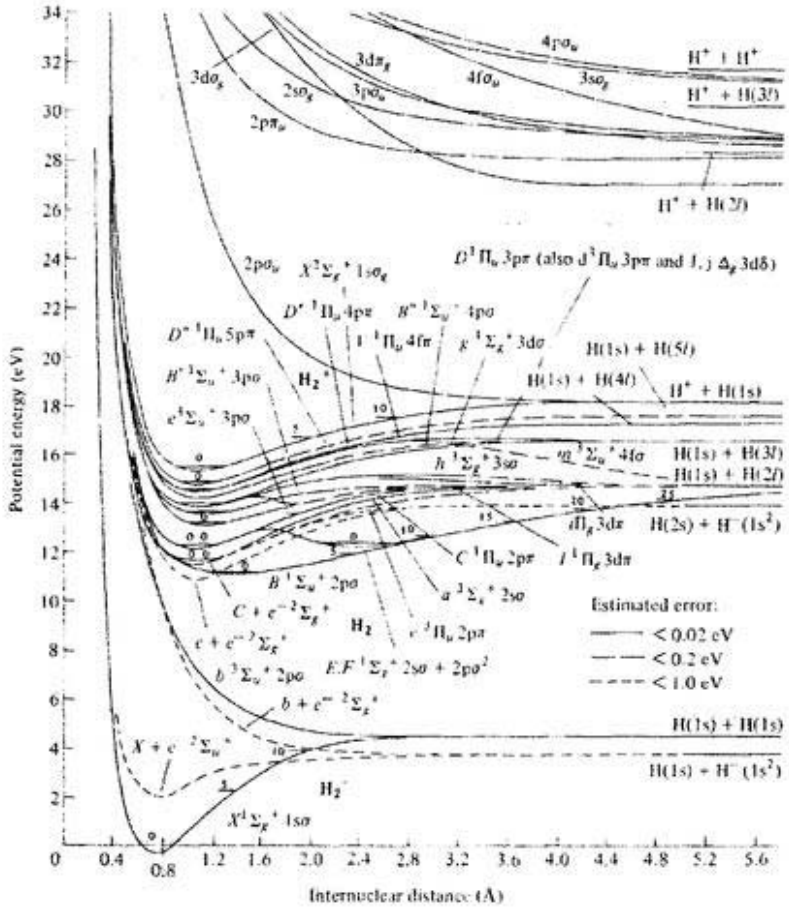

Figure 1.1: Potential-energy curves of H_2^- responsible for dissociative attachment in H_2. The broken curve is that for the ground Σ_g^+ state of H_2 from Ref. [6].

In 1970's, considerable H^- ions were detected in a hydrogen plasma [7][8], while no one could explain such experimental results by taking account of the production process of H^- ions via the dissociative attachment of electrons with molecules in the ground state [9]. Large ambiguity in

the measurement of H^- densities had made it difficult to discuss the production mechanisms of H^- ions in plasmas, owing to the limits of probe or mass spectroscopic measurements. Meanwhile, Langmuir probe combined with the laser photodetachment was developed to obtain more reliable measurements of H^- densities. This method is based on Langmuir probe measurements, in which a probe detects excess electrons released from H^- ions after photodetachment [10]. They could give an interpretation that existence of H^- ions in plasmas is attributed to the production of H^- ions from dissociative attachment of electrons to excited hydrogen molecules.

Cross sections for dissociative attachment to excited H_2 molecules were calculated theoretically by Wadehara et al. [11] to explain anomalous H^- densities in ion sources. They concentrated on their calculations for the following reaction;

$$e + H_2(X^1\Sigma_g^+, v) \rightarrow H_2^-(^2\Sigma_u^+, ^2\Sigma_g^-) \rightarrow H^- + H, \tag{1.1}$$

because it seemed to be the most probable reactions, as can be found from Fig. 1.1. It is clear that higher vibrational states of H_2 have a higher possibility for H^- production. The cross sections for dissociative attachment to excited H_2 molecules σ_{DA} were given as a function of the electron energy shown in Fig. 1.2 of Ref. [11]. These cross sections have been used to estimate the H^- density in an ion source. [12]

The densities of excited molecular hydrogen, $H_2(v'' < 5)$, and H atom were obtained by means of resonance-enhanced multiphoton ionization(REMPI) [13].

Formation of negative ions by surface production

H^- production on a metal surface has been studied for efficient productions in plasma sputter type ion sources and surface converter type ion sources, since the discovery by Krohn in 1962. The correlation between negative ion yield(Mo^-, as well as H^-) and work function on cesium adsorbate Mo surface was investigated by Yu in 1978 [14]. Figure 1.3 shows the dependence of Mo^- and work function change $\Delta\phi$ on cesium deposition time. The maximum Mo^- yield agrees closely with the minimum work function. From this correlation, they revealed the tunneling mechanism for the production of sputtered negative ions using the experimental data. Figure 1.4 shows the schematic diagram of a potential barrier between a metal surface and an adsorbate atom in the cases for (a) clean metal surface and (b) alkali metal adsorbate surface. In the case of (a), when an atom approaches toward a metal surface, the potential barrier between the atom and the metal suppresses electrons from escaping toward the adsorbate atom with the affinity level.

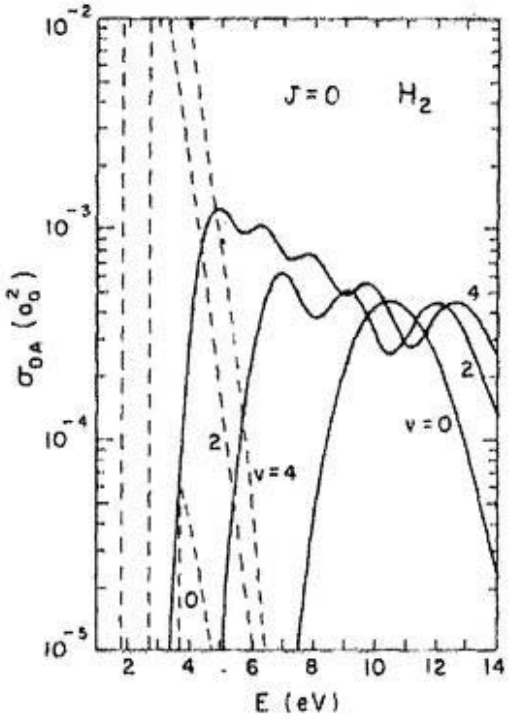

Figure 1.2: Dissociative attachment cross sections for various vibrational states(rotational states $J = 0$) of $H_2(—^2\Sigma_g^+, - - -^2\Sigma_u^+)$, calculated by Wadehara from Ref. [11].

When alkali metal is adsorbed on the metal surface(case (b)), the potential barrier becomes lower than that of (a) because of the lower Fermi level and lower work function of the metal. After all, this reduction of the potential barrier causes the increase of tunneling probability of electrons in the metal, and leads to the negative ion production. This theoretical model is given by Blandin et al.[15]. In the quantum mechanical model, the probability for a low velocity particle escaping from the surface as a negative ion can be given,

$$\beta^- \simeq \frac{2}{\pi} \exp\left[-\frac{\pi(\phi - S)}{2av_z}\right], \tag{1.2}$$

with the work function ϕ, the normal velocity v_z, the affinity energy S, and the exponential decay constant of the transition rate at large distances a.

Using this production mechanism, various ion sources have been developed. For surface converter type ion sources, Belchenko et al. reported that the surface production is the principal mechanism for H^- formation in 1973 [16]. Graham investigated the possible production mechanism of H^- and D^- ions sputtered from Cs adsorbate surfaces by measuring D^- yield and change

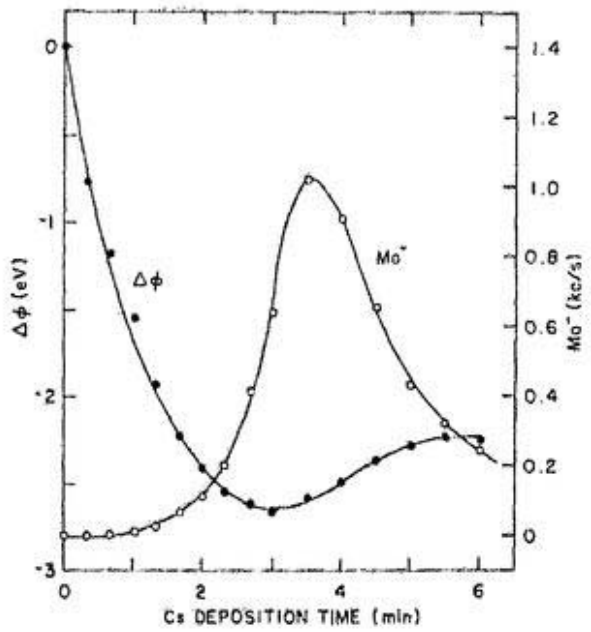

Figure 1.3: Dependence of Mo^- yield and work function change $\Delta\phi$ on cesium deposition time, measured by Yu from Ref. [14].

of work function. [17]

Hiskes et al. [18] discussed a model for the formation of negative ions by particles scattered from alkali-metal surfaces(Li, Na, K, Rb, Cs and the composite surface, Na-Cu). From the potential energy curves for CsH and CsH^- in Fig. 1.5, when a hydrogen atom approaches the cesiated surface, CsH is formed at a distance. As electrons are supplied from the cesiated surface due to tunneling, CsH getting an electron forms CsH^-, and leads to Cs + H^-. Their result in Fig. 1.6 also shows the clear dependence upon the work functions and the difference of H^- yield between various alkali metal adsorbed surfaces.

Charge exchange process from positive to negative ions

Negative ions are created by charge exchange;

$$A^+ + \text{neutral gas} \rightarrow A^-, A.$$

Cross sections for this reaction have dependence on the beam energy of A^+, and one must select the kind of gas or metal vapor for the high conversion rate and the efficient production. When negative ions do not have the volume production process and the surface production, this process

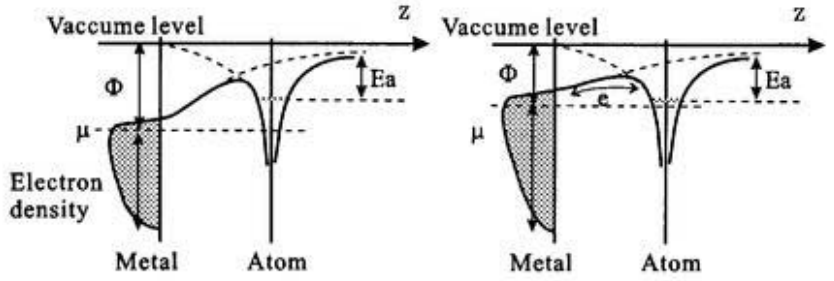

(a) clean surface (b) alkali metal adsorbate surface

Figure 1.4: Energy level diagram for the negative ion formation at an adsorbate metal surface. Φ is the work function of the metal, μ Fermi level, and Ea electron affinity.

is considered to be effective [19].

1.2 Ion sources for production of negative ions

Negative ion sources have been developed by using three production processes noted above.

In the present work we think of the production of H^- ions in a volume ion source. The volume production type negative ion sources of the present use for high energy and current requirement are schematically shown in Fig. 1.7. Since an ion source is filled with H_2 molecules, high energy electrons from filaments collide with ground level H_2 molecules in the driver region. Some H_2 molecules are excited to higher rovibrational levels $H_2(v'')$, and the rest transits to other states. The neutral particles produced in the driver region can move freely from magnetic filter fields. Low energy electrons pass through the magnetic field with positive ions by ambipolar diffusion to the extraction region. Consequently, there exist only low energy electrons($<$ 1eV) e_{slow} in the extraction region. H^- ions are produced abundantly by the dissociative attachment of e_{slow} to $H_2(v'')$, which is explained in Eq. (1.1), and are not destroyed by high energy electrons.

1.3 History of laser photodetachment technique

The spectroscopy of photodetached electrons gives us important information on negative ions. Many researchers have investigated the energy levels of metastable negative ions by means of the measurements of electrons detached from negative ion beams, since the first crossed-beam measurements were made by Branscomb et al. in 1954. The photodetachment cross-sections for various negative ions came to be measured more precisely with the development of light sources, especially laser lights, instead of arc discharge lamps.

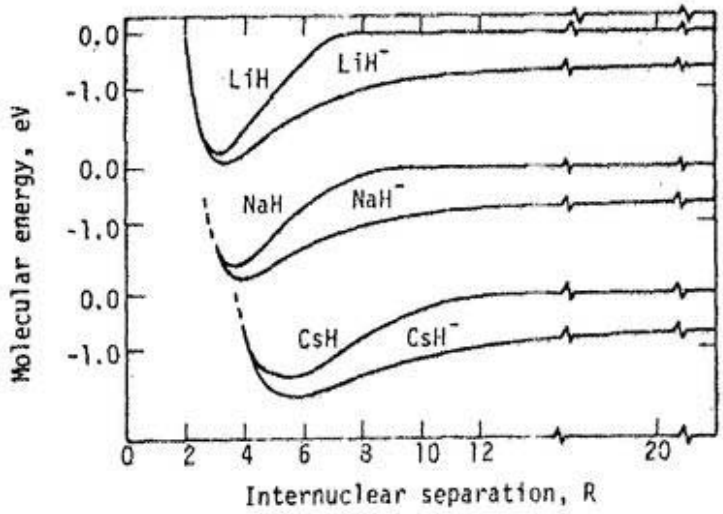

Figure 1.5: Potential-energy curves of H_2^- responsible for dissociative attachment in H_2. The broken curve is that for the ground Σ_g^+ state of H_2 from Ref. [18].

The photodetachment cross sections measured using negative ion beams are essential to H^- density measurement by photodetachment in plasmas, because the data of photodetachment cross sections for H^- ions give us an important information how much electrons are detached from H^- ions at a certain laser power density.

The photodetachment method associated with a Langmuir probe has been widely used to measure the H^- density, n_-, and temperature, T_-, in H_2 plasmas. Taillet measured negative ion density in oxygen plasmas using this method. By using a laser which has a photon energy larger than the electron affinity of hydrogen, electrons can be detached from H^- ions as the same principle as in a beam. A cylindrical Langmuir probe is located parallel to the laser beam and immersed into it to detect the excess electrons detached from H^- ions. Bacal et al. have shown in 1979 that the H^- density can be determined using this method [8, 10]. A few years later Stern et al. [20] have measured successfully the H^- temperature by making use of a double pulse laser, one of which is destroying all H^- ions and the other is delayed in time for searching the recovering H^- ions. They determined the thermal velocity and the temperature of H^- ions by using the ballistic model, in which the H^- ions return to the laser irradiated region with their thermal velocities to replace the photodetached electrons. This is called "monopolar drift" of H^- ions. In Ref. [20] it was also shown that the velocities obtained from (a) the time duration of photodetachment current signal, as measured earlier in Ref. [22], and from (b) the time delay

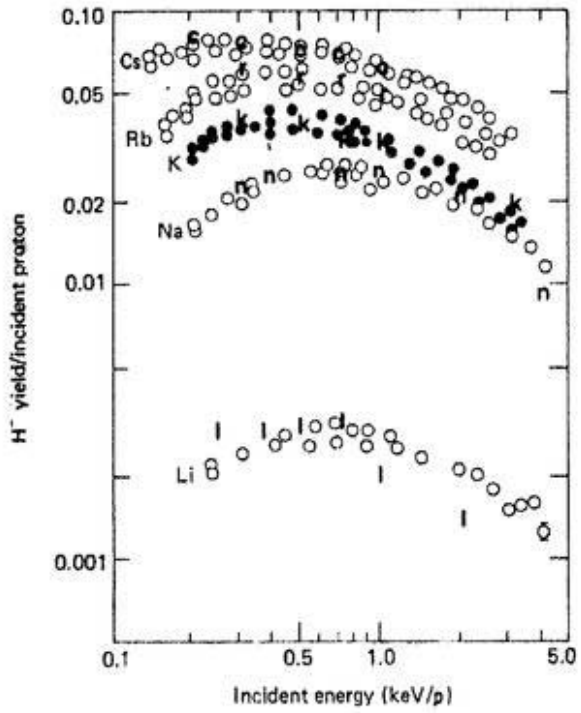

Figure 1.6: Backscattered H^- yield for molecular hydrogen ions incident on various alkali metal surfaces from Ref. [18].

between the laser beam and the photodetachment signal recorded by a probe located outside the laser beam were equal and corresponded to the thermal velocity of the H^- ions determined by the two-laser beam technique. Eenshuistra et al. [13] have also determined the H^- velocity from the duration of a single laser shot and showed that this velocity was equal, within 20 %, to the ion acoustic velocity of H_3^+ ions.

Other diagnostic methods for H^- ions are noted in chapter 2.1. The theoretical and experimental progress in photodetachment is mentioned in chapter 4.1.

1.4 Present work

Negative ions are widely used in various fields such as tandem accelerators, process plasmas for semiconductor etching, and heating devices of nuclear fusion. It is important to diagnose negative ion sources for the purpose of the optimization and high performance of negative ion production. In this study, we treat the laser photodetachment technique, which is considered to be one of the most useful techniques. Although the laser photodetachment technique has

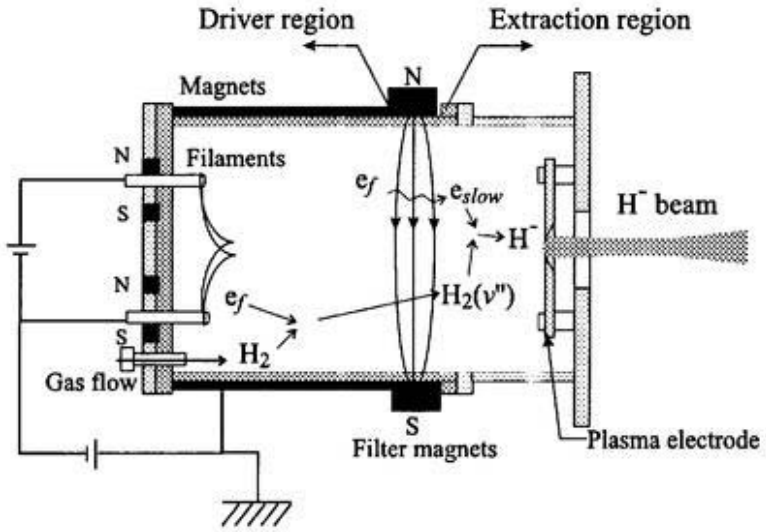

Figure 1.7: Volume production type negative ion source. Inside the source the volume is divided into two regions by magnetic filter fields. One is the driver region and the other is the extraction region.

been studied and utilized by many researchers, the influence of detached electron energies on measured parameters has not yet understood well. First, we investigate the space-temporal dependence of excess electrons generated by photodetachment on laser wavelength. From the results we verify whether the relations which give the negative ion density and temperature are appropriate or not. Next, the diagnostic technique for negative ions is established in consideration with a plasma perturbation induced by the laser photodetachment, and especially leads to the positive ion temperature as well as the negative ion parameters. The precision and the application limit of the ballistic theory and the hybrid fluid-kinetic theory are discussed, compared with the experimental results. The extension of this theory enables us to analyze the plasma responses not only inside but also outside a laser channel. From the measurements outside the laser channel, the possibility of the determination of negative ion densities is verified.

The rest of this study is the application of the laser photodetachment technique to the actual negative ion sources. It follows to discussions of the negative ion production processes in negative ion sources by using the plasma parameters obtained. In particular, since the enhancement of H^- beam current has been reported in the addition of cesium in an ion source, the influence of H^- ions on the cesium seeding will be discussed.

This thesis consists of 7 chapters.

In chapter 1, the historical background of negative ions, ion sources, and the laser photode-

tachment technique in plasmas and the purpose of this study are described. In chapter 2, the principles of the probe measurement, the laser photodetachment technique, and the work function measurement are noted.

In chapter 3, we have discussed the influences of laser wavelengths on plasma parameters in laser photodetachment. By use of the calculated results of Friedland et al., the positive ion temperature will be estimated from the overshoot signal of $\Delta I - t$ trace.

In chapter 4, the dynamics of excess electrons modeled by Friedland et al. is introduced, and extend to their analysis outside the laser channel. The calculated results of the plasma perturbations are compared with the experimental results.

In chapters 5 and 6, the laser photodetachment technique is applied to the ion source diagnostics, and then the H^- production mechanism is discussed in the case of the addition of alkali metal vapor in plasma. Although the amount of cesium is usually controlled by means of the relation between the oven temperature and the extracted beam current, we use the spectroscopic measurement for the purpose of the precise monitor of cesium vapor in the ion source. In the extraction region the correlation between negative ion densities and the work function of the plasma electrode is reported. As the different alkali metal vapor, rubidium vapor is introduced into the ion source in order to investigate the mass effect.

Finally in chapter 7, the conclusions of this thesis are described.

Bibliography

[1] B. M. Smirnov, 'Negative Ions', McGraw-Hill Inc., 1982.

[2] S. H. Massey, 'Negative Ions 3rd Ed.', Cambridge Univ. Press., 1976.

[3] G. J. Schulz, Phys. Rev. 113, 816(1959).

[4] D. Rapp, T. E. Sharp, and D. D. Briglia, Phys. Rev. Lett. 14(1965).

[5] G. J. Schulz, and R. K. Asundi, Phys. Rev. Lett. **15**, 946(1965).

[6] T. Sharp, "Potential Energy Diagram for Molecular Hydrogen and Its Ions," *Atomic Data*, Vol. **2** (Academic Press, New York, 1971), p.119.

[7] K. Prelec and Th. Sluyters, Rev. Sci. Instrum. **44**, 1451(1973).

[8] M. Bacal and H. J. Doucet, Rapport P. M. I. 650(1974).

[9] E. Nicolopoulou, M. Bacal, and H. J. Doucet, J. Physique, **38**, 1399(1977).

[10] M. Bacal and G. W. Hamilton, Phys. Rev. Lett. **42**, 1538(1979).

[11] J. M. Wadehara and J. N. Bardsley, Phys. Rev. Lett. **41**, 1795(1978).

[12] O. Fukumasa, J. Phys:D, **22**, 1668(1989).

[13] P. J. Eenshuistra, R. M. A. Heeren, A. W. Kleyn, and H. J. Hopman, Phys. Rev. A**40**, 3613(1989).

[14] M. L. Yu, Phys. Rev. Lett. **40**, 574(1978).

[15] A. Blandin, A. Nortier and D. W. Hone, J. Phys.(Paris) **37**, 369(1976).

[16] Yu. I. Belchenko, G. I. Dimov and V. G. Dudnikov, Izv. Akad. Nauk SSSR Ser. Fiz. **37**, 2573(1973).

[17] W. G. Graham, Phys. Lett. **73**, 186(1979).

[18] J. R. Hiskes and P. J. Schneider, Phys. Rev. B, **23**, 949(1981).

[19] M. Sasao, A. Taniike, M. Nishiura, and M. Wada Rev. Sci. Instrum. **69**, 1063(1998).

[20] R. A. Stern, P. Devynck, M. Bacal, P. Berlemont, F. Hillion, and J. Taillet, Phys. Rev. A**41**, 3307(1990).

[21] M. Nishiura, M. Sasao, and M. Bacal, J. Appl. Phys. **83**, 2944(1998).

[22] P. Devynck, J. Auvray, M. Bacal, P. Berlemont, J. Bruneteau, R. Leroy, and R. A. Stern, Rev. Sci. Instrum. **60**, 2873(1989).

[23] P. J. Eenshuistra, M. Gochitashvilli, R. Becker, A. W. Kleyn, and H. J. Hopman, J. Appl. Phys. **67**, 85(1990).

Chapter 2

Plasma diagnostics in negative ion source

2.1 Langmuir probe measurement

When we want to measure the plasma characteristics in an ion source, a Langmuir probe is usually used because of its simplicity and ease. The electrical properties obtained by the Langmuir probe give us important information on plasmas; the electron density and electron temperature. If collisions with neutral particles and a magnetic field exist, the analysis becomes complicated. Throughout this thesis the analysis for electron densities and temperatures is carried out in collisionless and unmagnetized region as mentioned below.

The typical $I-V$ curve of the Langmuir probe is illustrated in Fig. 2.1. The $I-V$ curves in the saturation region depend on the shape of the probe tip due to the edge effect of the sheath. The curve (a) is obtained by a cylindrical Langmuir probe and (b) is a planar probe. When the probe potential, V_p, is equivalent to the plasma space potential ,V_{sp}, the probe current, I_p, is generated by the thermal motion of electrons and ions;

$$I_p = I_i^{th} + I_e^{th}, \tag{2.1}$$

where I_i^{th} and I_e^{th} are the current flowing into the probe caused by the thermal motions of electrons and ions, respectively. Since the ion current is much smaller than the electron current, the electron saturation current becomes:

$$I = \frac{1}{4} e n_e v_e S_p. \tag{2.2}$$

Here S_p is the area of the probe, and v_e is the velocity of electrons. In case that the probe

potential is lower than the plasma space potential, the probe current becomes:

$$I = \frac{1}{4} e n_e S_p \left[v_i - v_e \exp\left(\frac{e\,(V_p - V_s)}{\kappa T_e} \right) \right]. \tag{2.3}$$

If the ion saturation current is taken away from the probe current, the electron current is

$$I_e = \frac{1}{4} e n_e S_p v_e \exp\left(\frac{-e\,(V_p - V_s)}{k T_e} \right). \tag{2.4}$$

The derivative of I_e with respect to V_p becomes

$$\frac{d \ln I_e}{dV_p} = -\frac{e}{k T_e}. \tag{2.5}$$

Thus T_e and I_{es} can be found from the slope of the electron current and the absolute velue of the electron current at the space potential. Substituting obtained T_e and I_{es} into Eq. (2.2), n_e is obtained. For practical uses, Eq. (2.2) is transformed to

$$n_e(\mathrm{cm}^{-3}) = 3.37 \times 10^{11} \frac{I_{es}(\mathrm{Amp.})}{S_p(\mathrm{cm}^2)\sqrt{T_e}(\mathrm{eV})}. \tag{2.6}$$

The application for getting T_e and n_e on Microsoft Windows has made it possible to process digital data of $I - V$ curves routinely, which are acquired by a personal computer with IEEE488.

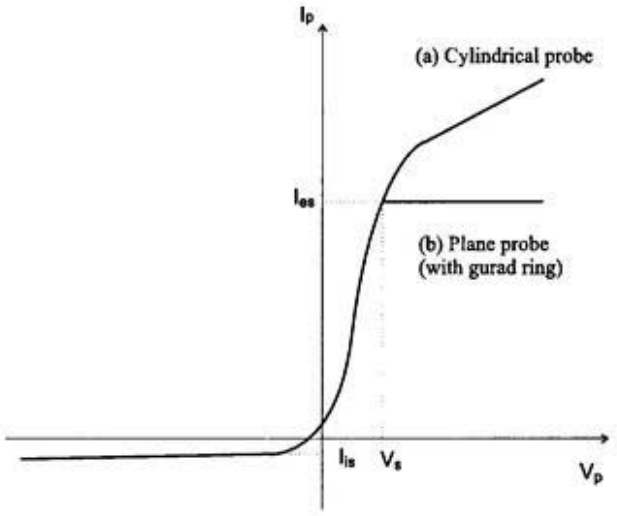

Figure 2.1: Typical probe $I - V$ characteristics of cylindrical probe and plane probe with guard ring.

There exists a difficult case to determine the electron saturation current and the plasma potential. The shape of the curve depends on the ratio of the probe radius, R, to the Debye length, λ_D. As R/λ_D approaches zero, the slope of the electron saturation current increases and

the plasma potential is not uncertain because of the edge effect of the sheath. Laframboise [1] carried out the numerical calculations of the electron and ion current captured by the spherical and the cylindrical probe under the collisionless and field free conditions.

If the abundant H^- ions exist in the plasma, it is pointed out that the effects of H^- ions on the sheath formation should be treated [2].

Negative ion densities given by the Langmuir probe theory are compared with those by the laser photodetachment technique experimentally and quantitatively by Nikitin et al. [3]. They have found that results by two methods are in reasonable agreement with each other, although the errors included in the electron and ion saturation current are much larger than those in the laser photodetachment technique. In particular, it is difficult to determine the negative ion density in plasmas, when the saturation region is smeared.

In oxygen plasma, the negative oxygen ions were detected from the second derivative of probe current, which consists of distribution functions for negative ions and electrons, when there exist negative ions [4]. The Druyvesteyn's method applied to the negative ion measurement was studied to introduce the n_-/n_e ratio. The peaks of the second derivative for negative ions, i''_{m-}, and for electrons, i''_{me}, correspond to the following relation [5],

$$\frac{i''_{me}}{i''_{m-}} = \frac{n_-}{n_e}\left(\frac{T_e}{T_-}\right)^{\frac{3}{2}}\left(\frac{m}{M_-}\right)^{\frac{1}{2}}. \tag{2.7}$$

Since Maxwellian distribution function for negative ions is assumed and T_- has to be determined, the measurement accuracy would be lower than that of the laser photodetachment technique. Moreover the probe material and the voltage fluctuation superimposed on the probe voltage change the sensitivity of the peaks. Solutions of these problems are required.

In a SF_6/Ar mixtured plasma, the n_-/n_+ fraction was obtained from the measurement of the velocity of ion acoustic waves by Onge et al. [6]. For the determination of n_-/n_+ fraction, ϵ, the following relation derived from the dispersion relation in three component plasma was used;

$$v'_\phi = C_s\sqrt{\frac{1}{1+k^2\lambda_{De}^2}\frac{1+\epsilon/M_r}{1-\epsilon}+3\tau} \pm U, \tag{2.8}$$

where τ is the ratio of ion to electron temperatures, T_i/T_e, M_r is the ratio of negative to positive ion mass, k is the wave number, λ_{De} is the electron Debye length, $C_s = \sqrt{\kappa T_e/M_+}$ is the ion acoustic speed, and U is the drift velocity of ion. In this case, $\tau \ll 1$ and $M_r \simeq 1$ were assumed to introduce Eq. (2.8). Their results indicate that the negative ion fractions are the same order and tendency as those given by the laser photodetachment technique. They conclude that the

ambiguity of the negative ion fraction is due to the inaccurate masses of molecular ions.

The laser photodetachment technique with a Langmuir probe, which is studied in this thesis, is considered to be more effective method. Instead of a Langmuir probe, the change of electron density after photodetachment can also be detected by plasma oscillation [7], microwave [8], laser interferometer technique [9], and absorption spectroscopy [10]. One needs to put proper use for them, since each technique presented above has its advantages and disadvantages.

2.2 Principle of negative ion density measurement by photodetachment

When a laser beam is irradiated to negative ions, electrons are released from negative ions, if the photon energy is in the range above the electron affinity of the atom. This reaction is called a photodetachment reaction:

$$A^- + h\nu \rightarrow A + e^-. \tag{2.9}$$

The cross section for photodetachment depends on the photon energy, as shown in Fig. 2.2.

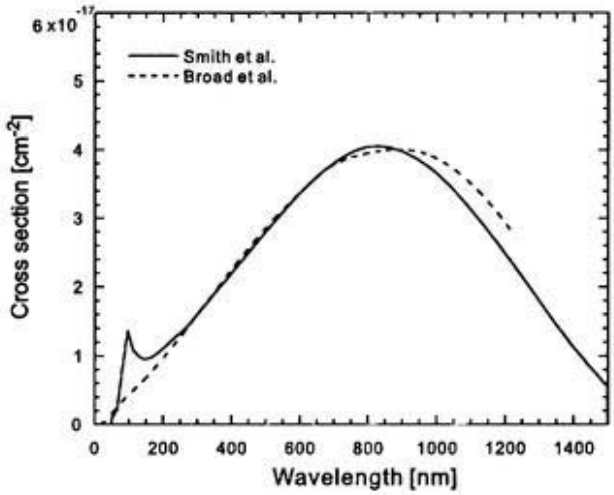

Figure 2.2: Cross section for photodetachment of an electron from H^-. Solid line is reproduced from ORNL data book [11] Broken line is the data calculated by Broad et al. [12]

The photodetachment rate of H^- ions, $\delta n_-/n_-$, depends on both the laser power and its wavelength, where δn_- is the fraction of the negative ion density destroyed by the laser photon. The $\delta n_-/n_-$ ratio is written as follows;[13]

$$\frac{\delta n_-}{n_-} = 1 - \exp\left(-\frac{W}{S_l}\frac{\sigma_{pd}}{h\nu}\right), \tag{2.10}$$

σ_{pd} : the cross section for photodetachment

W : the laser power

$h\nu$: the photon energy

S_l : the cross section of the laser beam

According to Eq. (2.10), if the enough laser power density is induced into the plasma, all the negative ions are destroyed in the laser channel, and then $\delta n_-/n_-$ saturates to nearly 1. The theoretical curves are compared with the experimental data in Fig. 3.4 of next chapter. We can confirm whether acquired data are attributed to photodetachment or not, by using Eq. (2.10).

Figure 2.3 shows a typical example of the photodetachment current superimposed on the electron saturation current. Then all the negative ions are destroyed by enough laser intensity. The signal has a slow rise time and a slow recovery time, compared with the transit time of thermal electrons. After 500 ns, the photodetachment signal returns to the initial level. When $\delta n_-/n_-$ is equal to 1, we can use the following relation to obtain the negative ion density; [13]

$$\frac{n_-}{n_e} = \frac{\delta n_e}{n_e} = \frac{\Delta I}{I_{dc}} \tag{2.11}$$

where I_{dc} corresponds to the electron current in the saturation region, and ΔI is the difference between I_{dc} and the maximum value of the electron current.

A. Inside the laser beam

After photodetachment, the electron density in the laser irradiated region increases immediately, while the H^- ions from the non-illuminated plasma flow into this region with a drift velocity, which is small compared to the thermal velocity of electrons. Then the H^- drift velocity is obtained from the recovery time of photodetachment current as the following; [14]

$$v_{drift} = \frac{R - R_p}{t_r} \tag{2.12}$$

where R is the laser beam radius, R_p is the collection radius, and the recovery time is t_r. The part below the original electron current is called "overshoot", I_{ov}.

B. Outside the laser beam

As shown in Fig. 2.4, the increase of the electron density due to photodetachment is also observed when the probe is located outside the laser beam with a time delay, Δt. After the

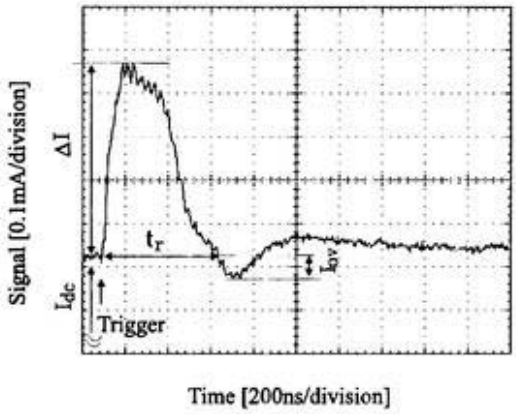

Figure 2.3: Time evolution of photodetachment signal on oscilloscope. The discharge condition is $V_d = 100$ V, $I_d = 6$ A, $P_g = 8.8$ mTorr, $W_L = 15$ mJ, and $\lambda = 532$ nm. Abscissa : time, 200 ns/division. Ordinate : 0.1 mA/division. Trigger in the figure indicates the trigger signal from the laser. The electron current of the probe I_{dc}, the maximum photodetachment current ΔI, the recovery time to the original current first t_r, and the overshoot signal below the original current I_{ov}, are defined respectively.

peak, the signal recovers to the initial level slowly with a larger time constant. Δt is increasing proportionally to the probe distance from the laser axis. The signal shows a slow rise and a slow decay at $r > R$, compared to those observed when the probe is located inside the laser beam. The velocity of the peak, v_b, becomes [15]

$$v_b = \left(\frac{dr}{d\Delta t}\right)_{r>R} \tag{2.13}$$

which is derived from the ballistic approximation. The details are noted in Appendix A.

2.3 Work function measurement

The adsorption of atoms and molecules on a surface influences the surface conditions significantly. As one of the methods for characterization of a surface, one can investigate changes in the work function of a metal surface, by measuring the photoelectron current. During the irradiation of a light to a metal surface, electrons, which obey the Fermi-Dirac statistics in a conduction band of the metal, absorb the photon energy, and then are excited to the higher level. If the energy of the light is higher than the gap to the vacuum level, electrons are emitted from the surface to the vacuum in a certain probability. Fowler has developed an analytical formula to relate the

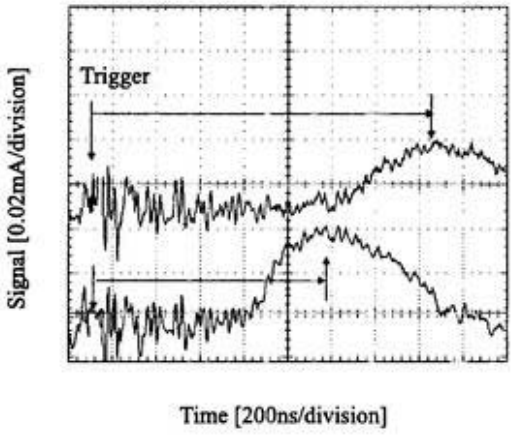

Figure 2.4: Variation of photodetachment signal outside the laser beam with $r = 6.0$ (lower trace) and 8.0 mm (upper trace). The discharge condition is $V_d = 100$ V, $I_d = 6$ A, $P_g = 8.8$ mTorr, $W_L = 15$ mJ, and $\lambda = 532$ nm. Abscissa : time, 200 ns/division. Ordinate : 0.02 mA/division. Trigger is the trigger signal of laser.

photoelectron current with the work function. The quantum efficiency is defined as follows:

$$Y = \frac{photoelectron\ \ number}{absorbed\ \ photon\ \ number}. \tag{2.14}$$

Assuming that electrons in a conduction band would obey the Fermi-Dirac distribution, the number of electrons per unit volume becomes

$$n = \frac{4\sqrt{2}\pi m^{3/2}k^2T^2a}{h}\int_0^\infty \frac{\log\left(1+\exp\left[-y+\left(h\nu-\Phi_w\right)/kT\right]\right)}{\sqrt{y+\left(U_0-h\nu\right)/kT}}dy \tag{2.15}$$

In the limit $T \to 0$, the relation between the quantum efficiency and the work function is given approximately by [16]

$$\begin{aligned} Y &\propto \frac{\left(h\nu-\Phi\right)^2}{\left(U_0-h\nu\right)^{\frac{1}{2}}} \quad , \text{if } h\nu > \Phi, \\ Y &= 0 \qquad\qquad\qquad\quad , \text{if } h\nu < \Phi, \end{aligned} \tag{2.16}$$

where U_0 is the potential step, and Φ work function of the surface. In order to determine the work function from the photoelectron current $I_{p.e.}$, the threshold of photoelectron current is usually measured by changing the wavelength of light(for example;Xe arc lamp et al.). In the case of Cs adsorbed Mo, a typical curve of work function changes is shown as a function of Cs thickness in Fig. 2.5. This result is measured under the condition of ultra high vacuum. Although the advantage of the precision for this method is fairly obvious, we use the one/two wavelength photoemission technique in order to measure Φ and n_-/n_e simultaneously.

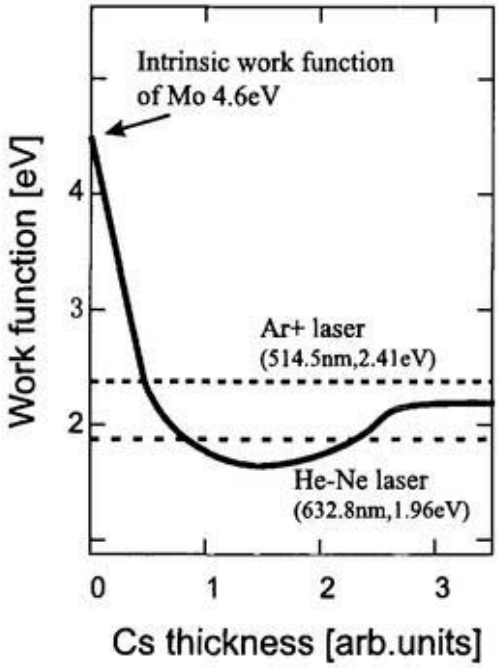

Figure 2.5: Typical changes of work function vs Cs thickness in the case of Cs adsorbed on a Mo surface. [18]

We have to know the relation between the photoelectron current and the work function. We introduce α as a constant value, and then Eq. (2.16) is rewritten by

$$\Phi = h\nu - \zeta I_{p.e.}^{1/2}, \tag{2.17}$$

where we assumed that U_0 and $h\nu$ would be a constant value in the experimental condition. The factor ζ must be determined. The maximum change of work function $\Delta\Phi$ for alkali and alkali-earth adsorption on a metal surface is estimated by the empirical formula [17]

$$\Delta\Phi = -1.24\left[\phi_0 - \frac{1}{2}(I_a + E_a)\right], \tag{2.18}$$

where ϕ_0 is the intrinsic work function, I_a is the first ionization energy, and E_a is the electron affinity of the adsorbed material. $\Delta\Phi$ for the alkali metal adsorption on a molybdenum surface is summarized in Table 2.1. Substituting the minimum work function $\Phi_{min}(= \phi_0 + \Delta\Phi)$ and maximum of $I_{p.e.}$ into Eq. (2.17), we can determine the factor α and translate the measured photoelectron current into the work function. The minimum work function of the cesium adsorbed molybdenum surface is estimated to 1.6 eV. When $I_{p.e.}$ is nearly equal to the threshold of the photoelectron emission, the signal of $I_{p.e.}$ is very low and is buried within the noise. On the other hand, we can determine the work function more precisely by means of the photoelectron emission

from two-laser lights [19]. The actual experimental circuit for the work function measurement is shown in Fig. 6.2 of chapter 6.

Table 2.1: Properties of alkali metal and work function changes $\Delta\Phi$.

	Mass	ϕ_0	E_a	I_a	$\lvert\Delta\Phi\rvert$ (Alkali/Mo)
Li	6.9	2.9	0.620	5.39	1.98
Na	23.0	2.75	0.548	5.14	2.18
K	39.1	2.30	0.501	4.34	2.70
Rb	85.5	2.16	0.486	4.18	2.81
Cs	132.9	2.14	0.472	3.89	3.00

The intrinsic work function of a Mo surface, $\phi_0 = 4.6$ eV, is used. E_a the electron affinity, I_a the ionization energy, and $|\Delta\phi|$ the work function reduction of alkali metal on Mo.

Bibliography

[1] J. G. Laframboise, UTIAS report NO.100, Univ. of Tronto,(1966).

[2] I. Arikata, and T. Kubota, Plasma kakuyugo gakkai, **74**, 160(1998).

[3] A. G. Nikitin, F. EI. Balghiti, and M. Bacal, Plasma Sources Sci. Technol. **5**, 37(1996).

[4] J. B. Thompson, Proc. Phys. Soc. **73**, 818(1959).

[5] H. Amemiya, J. Phys. Soc. of Japan **57**, 887(1988).

[6] L. St-Onge, J. Margot, and M. Chaker, Appl. Phys. Lett. **72**, 290(1998).

[7] T. H. Ahn, K. Nakamura, and H. Sugai, Jpn. J. Appl. Phys. **34**, 1405(1995).

[8] K. E. Greenberg, G. A. Hebner, and J. T. Verdeyen, Appl. Phys. Lett. **44**, 299(1984).

[9] C. Schiffer, and J. Uhlenbusch, Plasma Sources Sci. Technol. **4**, 345(1995).

[10] E. Quandt, H. F. Döbele, and W. G. Graham, Appl. Phys. lett. **72**, 2394(1998).

[11] ORNL data book, ORNL-DWG 75-7881. These data are refered from L. M. Branscomb and S. J. Smith, Phys. Rev. **98**, 1028(1955); S. J. Smith and D. S. Burch, Phys. Rev. **116**, 1125(1959); D. Feldman, Z. Naturforsch. 25-1, 621(1970); J. Macek, Proc. Phys. Soc. **92**, 365(1967); L. M. Branscomb,"Physics of the One- and Two-Electron Atoms", pp.669-699, North-Holland Publishing Co. (Amsterdam)(1969).

[12] J. T. Broad, and W. P. Reinhardt, Phys. Rev. **A14**, 2159(1976).

[13] M. Bacal and G. W. Hamilton, Phys. Rev. Lett. **42**, 1538(1979).

[14] P. Devynck, J. Auvray, M. Bacal, P. Berlemont, J. Bruneteau, R. Leroy, and R. A. Stern, Rev. Sci. Instrum. **60**, 2873(1989).

[15] R. A. Stern, P. Devynck, M. Bacal, P. Berlemont, F. Hillion, and J. Taillet, Phys. Rev. A**41**, 3307(1990).

[16] R. H. Fowler, Phys. Rev. **38**, 45(1931).

[17] G. D. Alton, Nucl. Instrum. Method. B**37/38**, 45(1989).

[18] M. Wada, Ph.D thesis, U. C. Berkeley(1983).

[19] Y. Okabe, M. Sasao, H. Yamaoka, M. Wada and J. Fujita, Jpn. J. of Appl. Phys. **30**, 1307(1991).

Chapter 3

H^- photodetachment in a plasma

3.1 Introduction

It is important to investigate the transport and the behavior of photodetached electrons in the plasma, since the photodetachment current must be influenced by the incident energy of photodetached electrons, especially at the sheath edge of the probe. Therefore the variation of the photon energy is an effective method to understand the mechanism of capture of photodetached electrons by a probe.

As shown in Ref. [1], the excess electrons recorded after photodetachment are not necessarily those produced originally by photodetachment. Some photodetached electrons are trapped in the potential well formed in the laser irradiated region and are thermalized, and some might be replaced by the background electrons of the plasma. However, the total number of excess electrons in the unit volume of the laser irradiated region is the same as that of the H^- ions destroyed by the laser, before the H^- density recovers due to H^- ions drifting from the background, non-illuminated plasma.

In this chapter, the effects of the photon energy on various characteristics are studied by single pulse photodetachment. We use the Nd-YAG fundamental wavelength and its second and third harmonics. The photon energy could thus be increased by a factor of three.

The change, due to the use of different photon energy, in the δI_p - V_p characteristic (δI_p is the amplitude of the photodetachment signal, V_p is the potential applied to the probe) in the retarding region is measured in order to study the effective temperature of the photodetached electrons captured by the probe and the dependence on the photon energy. We also study that there is no dependence of the H^- density and H^- drift velocity on the laser photon energy and compare them with the ion acoustic velocity of H_3^+.

We have also studied the effect of the photon energy on the amplitude of the "overshoot" present in the photodetachment signal. This overshoot is explained by using the theory of plasma response in Refs. [2] and [3]. In Ref. [2] it was shown that the magnitude of the overshoot was sensitive to the ratio of the positive ion to electron temperatures. From the data obtained by measuring the dependence of the overshoot on H_2 gas pressure and on the photon energy are shown for the purpose of the discussions on the volocity.

3.2 Experimental setup and method

The schematic diagram of the experimental apparatus is shown in Fig. 3.1. The discharge chamber is a stainless-steel vessel of 270 mm in length and 210 mm in diameter. Ten rows of ferrite magnets, surrounding the vessel, and four ferrite magnets on the end plate are arranged to produce a multicusp magnetic field for plasma confinement. The magnetic field is about 300 Gauss on the wall surface and a few Gauss at the center of the vessel. Since the H^- density and the H^- drift velocity are measured at the center of the vessel, the influence of the magnetic field is negligible. Two Tungsten filaments attached to current feedthroughs located on the end plate generate primary electrons. Hydrogen gas is admitted into the ion source through a port in the center of the end plate. The gas pressure is monitored by using an ionization gauge.

The holder of a cylindrical Langmuir probe is installed perpendicularly to the laser beam. The tip of the L-shaped probe, which is made of a tungsten wire, is 10 mm in length and 0.35 mm in diameter, as illustrated in Fig. 3.2. It is movable from 0 to 15 mm in the radial direction r of the cylindrical vessel by using a micrometric screw. The signal line is shielded perfectly in a coaxial construction to avoid an external noise. The electron density, n_e, and the electron temperature, T_e, at the central region of the ion source, measured with the Langmuir probe, are shown in Fig. 3.6. The electron density varies from 10^{10} cm^{-3} to 10^{11} cm^{-3} and the electron temperature from 3 to 0.5 eV, when the hydrogen gas pressure varies from 0.4 to 18 mTorr. The H^- density is discussed in section 3.3.3.

In this experiment a Nd-YAG laser(Lambda Physik, LPY150) is used to detach electrons from H^- ions. The pulse duration of the laser beam is 3.3 ns. It is much shorter than the duration of the photodetachment signal, which in the example of Fig. 2.3 lasts 800 ns . Three different laser wavelengths of 1064, 532 and 355 nm can be produced by the harmonic generator mounted on the laser head. Harmonic separators are used to separate three mixed laser wavelengths. The laser

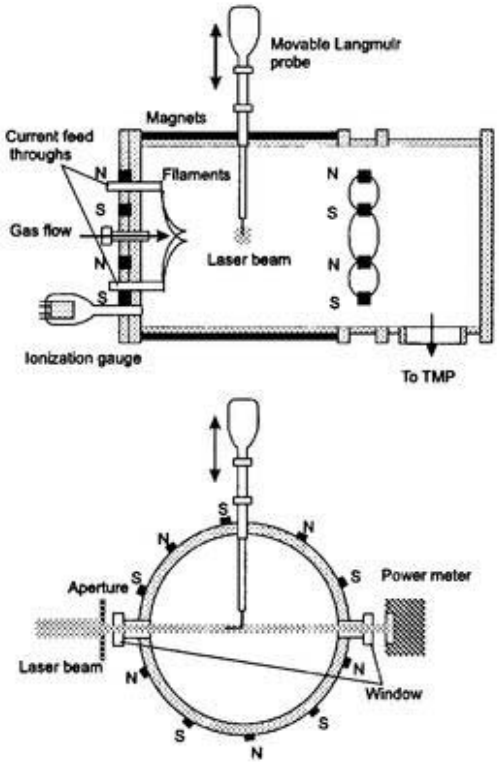

Figure 3.1: Illustrations of the multicusp ion source and the set up for the photodetachment measurement.

diameter is limited to 4 mm to maintain the uniformity of the laser photon density. This is done by locating a suitable aperture in front of the window of the discharge chamber. The laser power at the exit of the plasma chamber is measured by a photodiode type power meter(Scientech, PHD50), calibrated for each wavelength.

The L-shaped probe is connected to the probe power supply through the resister as shown in Fig. 3.3. The probe current is monitored with the 50 Ω resister and the potential with the output power of the power supply, where digital multimeters(DMM, ADVANTEST:R6451A) are used. In the case of $I-V$ measurements, the probe power supply and DMMs are controlled by a PC-AT compatible computer with GP-IB card bus. When a photodetachment signal is measured, the probe power supply is fixed at a certain positive voltage. Only a signal synchronized with the trigger of the laser is stored by the digital storage scope(Sony Tektronics:TSD684A)

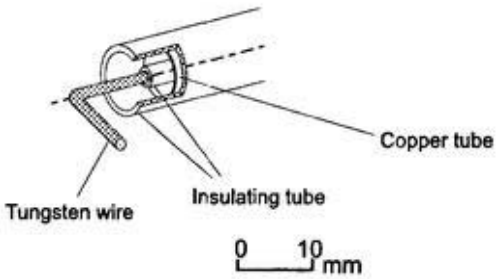

Figure 3.2: Illustrations of L-shaped Langmuir probe.

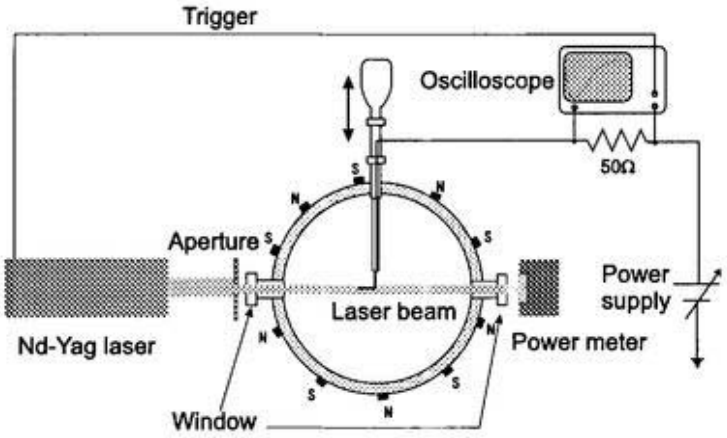

Figure 3.3: Illustration of electrical circuit for the photodetachment experiment.

3.3 Results and Discussions

3.3.1 Dependence of the photodetachment rate on laser power and wavelength

The photodetachment current is plotted as a function of laser power for different laser wavelength, λ_L, in Fig. 3.4. Each curve shows the theoretical values of Eq. (2.10) in the case of $\lambda_L = 1064$ nm, 532 nm and 355 nm, respectively. The photodetachment cross sections of H^- ions in Ref. [4] are used to calculate the theoretical curves. Higher laser power is required to get the saturation of photodetachment signal for the shorter laser wavelength. The experimental data are in close agreement with the theoretical prediction, except the lower power region, where the laser power is unstable.

The good agreement of the measurements with the theoretical curves also indicates the absence of some impurities. For example, oxygen molecules and atoms may be present in the discharge

chamber. The electron affinity is 1.46 eV for O^-, 0.44 eV for O_2^- and 2.1 eV for O_3^-. The photon energies corresponding to the 2nd and 3rd harmonic are 2.4 eV and 3.6 eV. They are high enough to detach electrons from O^- ions and O_3^-, while the photon energy of the fundamental beam (1064 nm) is not.

The experiments described below are obtained in the saturation region of photodetachment current.

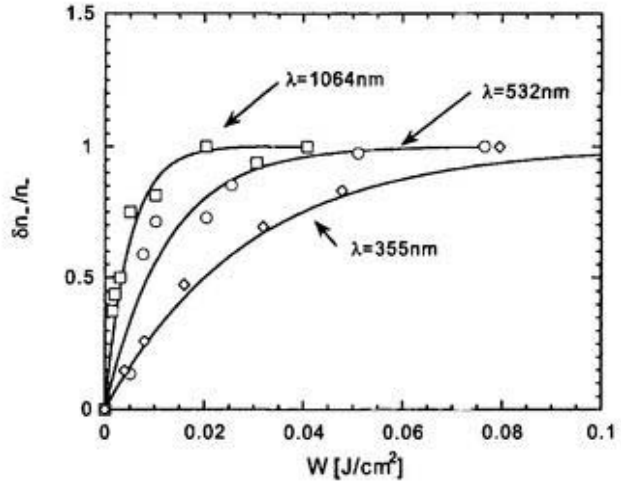

Figure 3.4: Comparison of photodetachment rate, $\delta n_-/n_-$, with theoretical curves. Three lines in this figure indicate the theoretical curves of Eq. (2.10)

3.3.2 Dependence of the photodetachment current on probe voltage

The characteristics of normalized probe current, $\tilde{I}_p$ and photodetachment current, $\delta\tilde{I}_p$ from the fundamental beam (1064 nm) and the 2nd harmonic beam (532 nm) on probe potential V_p are shown in Fig. 3.5(a) and (b), respectively. Line and circles show $\tilde{I}_p$ and $\delta\tilde{I}_p$, respectively. Each current is normalized to unity in the saturation region. In the retarding region the slope of $\delta\tilde{I}_p$ is different from that of $\tilde{I}_p$. $\delta\tilde{I}_p$ emerges near the plasma potential, where the probe current disagrees with the exponential fitting curve. Although the energy of photodetached electrons is 0.425 eV for 1064 nm and 1.59 eV for 532 nm, the characteristic of the measured $\delta\tilde{I}_p$ in Fig. 3.5(a) is similar to that in Fig. 3.5(b). If we assume that the distribution of the photodetached electrons becomes Maxwellian, the effective temperature of photodetached electrons T_{eff} is roughly 0.5 eV for the fundamental and the 2nd harmonic from the slope of this curve, which is lower than the background electron temperature 0.86 eV at the H_2 gas pressure. In this case T_e/T_{eff} is

about 1.7. When the H_2 gas pressure is decreased, the ratio, T_e/T_{eff}, tends to preserve this constant value. There is no influence of the photon energy on T_{eff} and on the absolute value of the photodetachment current. If δI_e would reflect the Maxwellian distribution of H^- ions before photodetachment, the slope of δI_e is given by

$$\delta I_e \propto n_-(\phi) = n_- \exp\left(-\frac{e\phi}{kT_-}\right). \tag{3.1}$$

The slope is constant and becomes:

$$\frac{d\ln \delta I_e}{d\phi} = -\frac{e}{kT_-}. \tag{3.2}$$

T_- obtained from Eq. (3.2) tends to be twice higher than that from the drift velocity of H^- ions. Further studies on this problem are needed.

The Maxwellization time of electrons τ_{Me} [1] is an important parameter when the distribution function of the photodetached electrons is considered. In a typical ion source plasma, the Coulomb logarithm Λ is 10, and $n_e = 10^{10} \sim 10^{11}$ cm^{-3}, τ_{Me} becomes of the order of 64 $\sim$ 640 ns for the fundamental, and 460 $\sim$ 4600 ns for the 2nd harmonic. In both cases τ_{Me} is larger than the rise time of the photodetachment current, which is typically less than 200 ns, as will be shown in Sec. 3.3.4. Therefore the photodetached electrons are not thermalized in the present experiments, but electrons can be replaced by the background electrons. Then we may assume T_{eff} is close to T_e and it is independent of the photon energy. This assumption is used for the evaluation of H^- density. More precise data are needed for the well-understanding of the physics based on this phenomena.

The plasma potential is obtained by analyzing the probe $I - V$ characteristics. Apparently, there is no difference between the photodetachment current curve at 1064 nm and that at 532 nm. The photodetachment current rises up at the plasma potential. The plasma potential minus the potential at the zero photodetachment current does not agree with the energies of photodetached electrons. This is also caused by the apparent replacement of photodetached electrons with background electrons.

3.3.3 Dependence of the electron density and the H^- density on H_2 gas pressure

The dependence of the negative ion density on H_2 gas pressure in the case of using the laser wavelengths of 1064 nm and 532 nm is shown in Fig. 3.6. The H^- density is obtained by using Eq. (2.11). The electron density varies from 10^{10} cm^{-3} to 10^{11} cm^{-3} and the H^- density from 10^8

cm^{-3} to 10^9 cm^{-3}. No dependence on the photon energy is observed in n_e, n_{H^-}, nor T_e. As we increase the H_2 gas pressure, both the electron density and the H^- density increase until 5 mTorr. The H^- density reaches the maximum value at 5 mTorr and goes down slowly, while the electron density is saturated at 10 mTorr. The collisions with neutral gas would be dominant at high gas pressure. For a volume production type negative ion source, the maximum value of the H^- density results from the balance between the collisional destruction and the production through the dissociative attachment of low energy electrons with vibrationally excited H_2 molecules.

3.3.4 Comparison between H^- drift velocities determined with a probe inside and outside the laser beam.

By using Eq. (2.12), the dependence of the H^- drift velocity on H_2 gas pressure is obtained in Fig. 3.8(a), when the probe is located on the axis of the laser beam. Three laser wavelengths are used to detach electrons from H^- ions. The H^- drift velocity increases from 2.5×10^3 m/s to 8×10^3 m/s, when the electron temperature increases from 0.5 eV to 3 eV, and has almost the same value at each wavelength studied. The H^- drift velocity is lower than that which could be obtained by $h\nu - \varepsilon_a$. In Fig. 3.8(a) the acoustic velocities for H^+, H_2^+ and H_3^+ are also calculated using the following equation [6] and the measured electron temperature;

$$C_s = \sqrt{\frac{\kappa T_e}{M_n}} \qquad n = 1, 2, 3, \tag{3.3}$$

where n = 1, 2 and 3 indicate the ion mass for H^+, H_2^+ and H_3^+. The H^- drift velocity is very close to the ion acoustic velocity of H_3^+.

In the case of measurement outside laser beam, the drift velocity is calculated by use of Eq. (2.13). The measured time delay Δt is shown in Fig. 3.7 as a function of probe distance r. To obtain the drift velocity of H^- ions the slope of the $\Delta t - r$ curve in Fig. 3.7 can be used.

The dependence of the drift velocity on H_2 gas pressure is shown in Fig. 3.8(b). The drift velocity varies from 8×10^3 m/s to 2.5×10^3 m/s with the gas pressure, and has almost the same value at each wavelength. The drift velocity is also very close to the ion acoustic velocity for H_3^+. There is almost no difference between the drift velocities plotted in Fig. 3.8(a) and (b) except in the low pressure region, in which there is large ambiguity due to the small signals of photodetachment current. It is concluded that the outward flow of electrons occurs at the same velocity as the inward flow of negative ions, as assumed in the monopolar transport model [5]. In addition, it is considered the main component of positive ions in the plasma is almost H_3^+, which is consistent with the results of extraction experiments in Ref. [7].

From the result of v_b, the estimate of the negative ion temperature T_- is carried out and the results are shown as a function of T_e in Fig. 3.9. T_- is naturally in an agreement with each laser wavelength. The variation rate of T_- is comparably smaller than that of T_e and is not linearly, especially in the region, where T_e is larger than the electron affinity of hydrogen. It suggest that T_- dependence on T_e is related with the formation of H^-.

3.3.5 Dependence of the overshoot signal on the laser wavelength

The overshoot current I_{ov} is the difference between the second peak and the background current, as shown in Fig. 3.10. I_{ov} and ΔI are very sensitive to the discharge conditions. The dependence of the overshoot and the photodetachment current on H_2 gas pressure is shown in Fig. 3.10(a). We have noted that the overshoot signal does not depend on the laser photon energy. When the H_2 gas pressure exceeds 4.4 mTorr, the overshoot signal dumps gradually. As mentioned in next chapter, the overshoot signal becomes larger with higher T_+/T_e. The dependence of the $I_{ov}/\Delta I$ ratio on H_2 gas pressure is shown in Fig. 3.10(b). The $I_{ov}/\Delta I$ ratio does not depend on the electron density, the H^- density and the laser wavelength.

Using the data from Fig. 3.10(a) and Fig. 3.6, we plotted in Fig. 3.11 the variation of the overshoot signal amplitude with the electron temperature. We also plotted the theoretical curve from Ref. [2] in this figure, assuming that the positive ion temperature, T_+, is 0.1 eV. A good agreement with theory is found using a reasonable value for the positive ion temperature. The variation of the positive ion temperature is very small because of their large mass compared to electrons. However since the negative ions are produced from the attachment of the thermal electrons, the variation of the H^- temperature is larger than that of the positive ions.

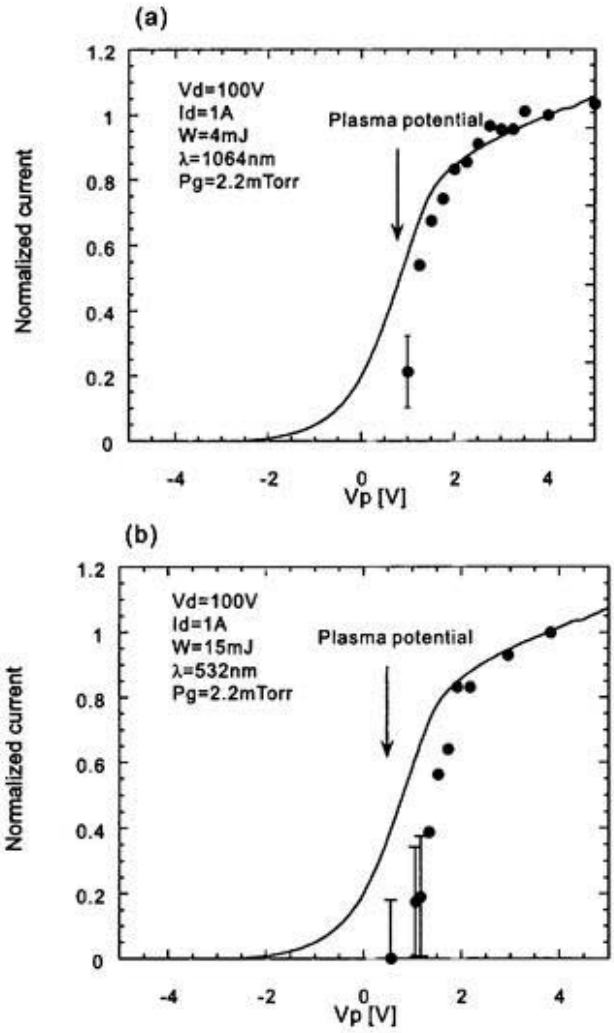

Figure 3.5: Dependence of the probe and the photodetachment current on the probe potential.(a)λ = 1064 nm and W_L = 4 mJ. (b)λ = 532 nm and W_L = 15 mJ. In both cases the discharge conditions were V_d = 100 V, I_d = 1 A, and P_g = 2.2 mTorr.

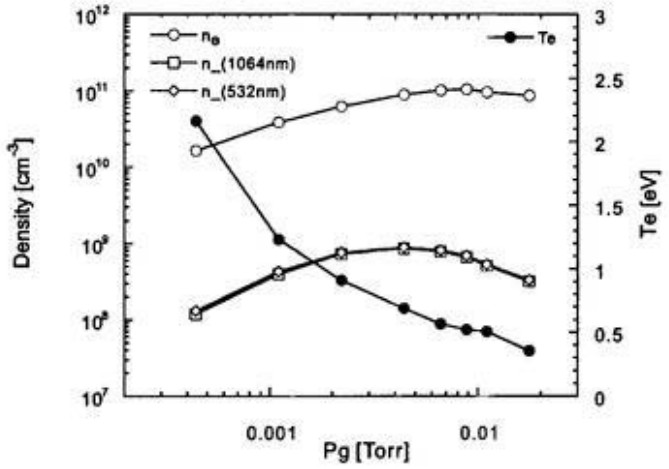

Figure 3.6: Plasma parameters(electron, negative ion densities, and electron temperatures) under the conditions of $I_d = 1$ A and $V_d = 100$ V. The comparisons of different wavelengths are also plotted at 532 and 1064 nm.

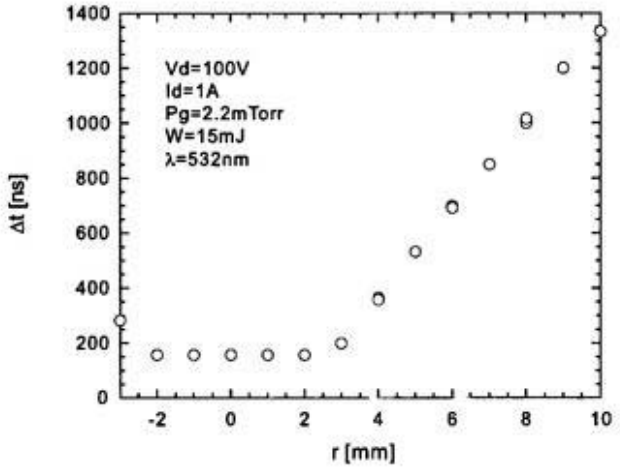

Figure 3.7: Variation of delay time Δt with probe position r along diametral chord. The laser diameter, $2R$, is 4 mm.

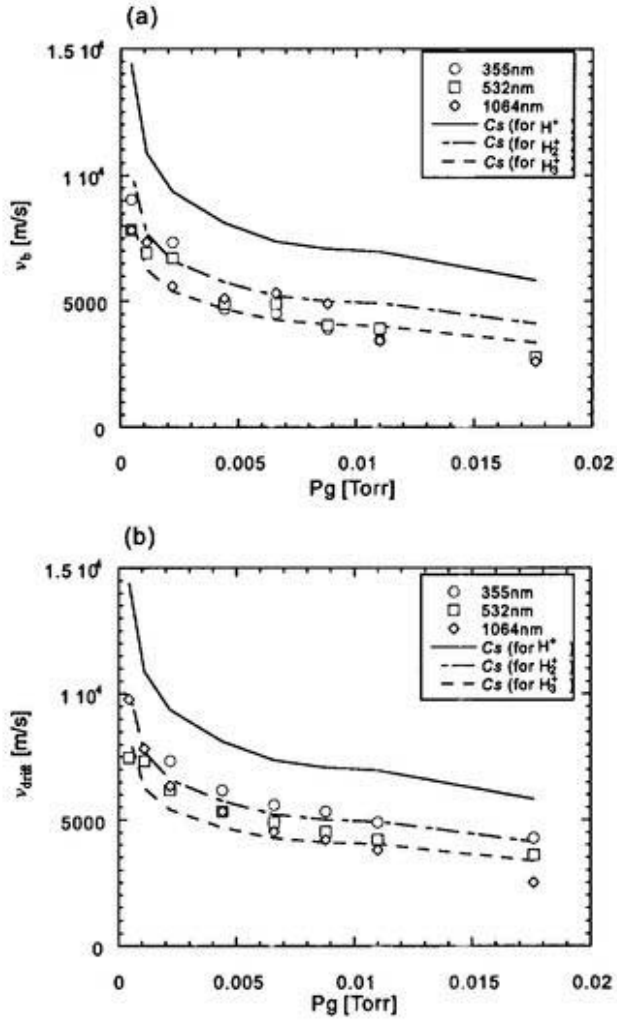

Figure 3.8: (a)Dependence of the H^- drift velocity obtained from the transition time Δt on hydrogen gas pressure. The ion acoustic velocities C_s are also plotted at various species of positive ions(H^+, H_2^+, and H_3^+) under the conditions of $I_d = 1$ A and $V_d = 100$ V. The comparisons of different wavelengths($\lambda = 355$, 532, and 1064 nm) are also plotted. (b)The H^- drift velocity obtained from the recovery time.

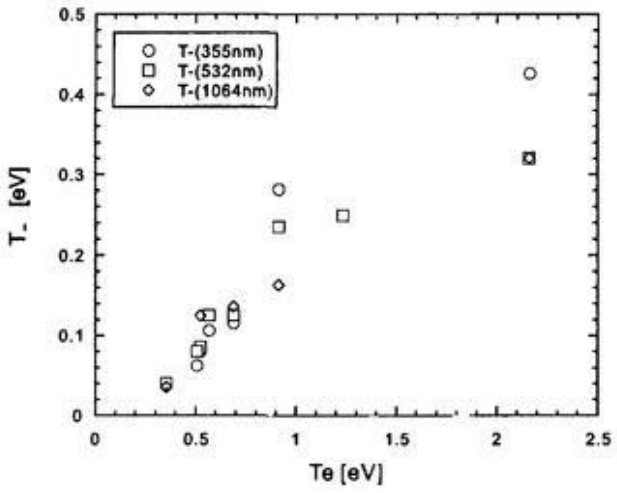

Figure 3.9: Relation between H^- and electron temperatures under the conditions of $I_d = 1$ A and $V_d = 100$ V. The comparisons of different wavelengths($\lambda = 355$, 532, and 1064 nm) are also plotted.

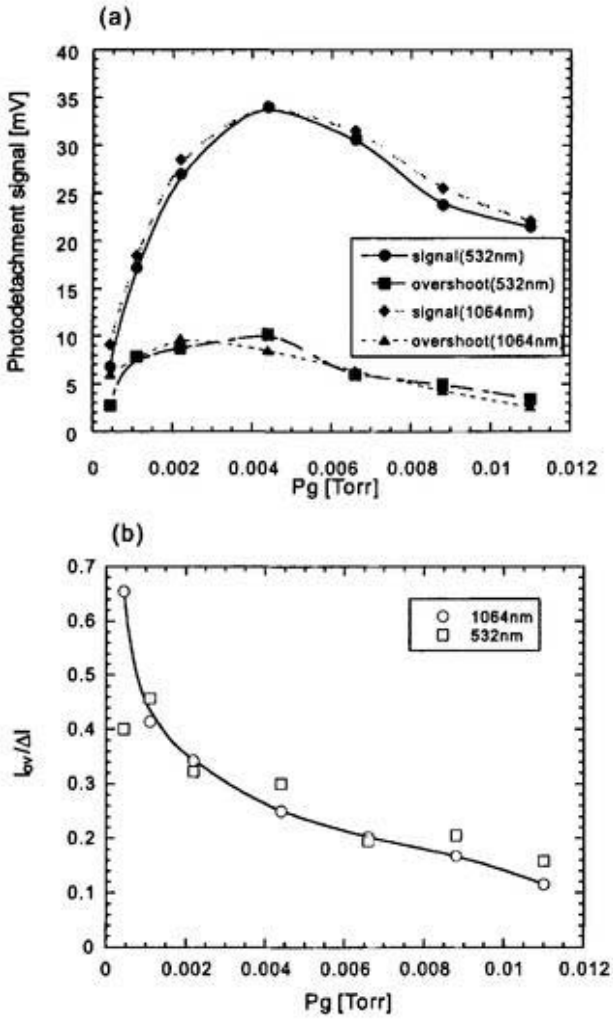

Figure 3.10: (a)Dependence of the overshoot of photodetachment current on hydrogen gas pressure under the conditions of $I_d = 1$ A and $V_d = 100$ V. (b)Dependence of the $I_{ov}/\Delta I$ ratio on hydrogen gas pressure. The comparisons of different wavelengths($\lambda = 355$, 532, and 1064 nm) are also plotted.

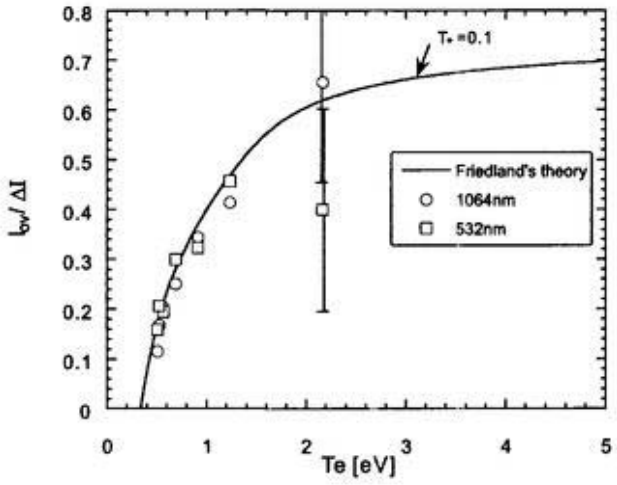

Figure 3.11: Comparison of the measured $I_{ov}/\Delta I$ ratio with Friedland's theory in Ref. [2], in which the data of photodetachment signals are calculated by the hybrid fluid kinetic model.

Bibliography

[1] F. El Balghiti-Sube, F. G. Baksht and M. Bacal, Rev. Sci. Instrum. **67**, 2221 (1996).

[2] L. Friedland, C. I. Ciubotariu, and M. Bacal, Phys. Rev. **E49**, 4353(1995).

[3] A. A. Ivanov, L. I. Elizarov, M. Bacal, and A. B. Sionov, Phys. Rev. **E52**, 6679(1995).

[4] J. T. Broad, and W. P. Reinhardt, Phys. Rev. **A14**, 2159(1976).

[5] R. A. Stern, P. Devynck, M. Bacal, P. Berlemont, F. Hillion, and J. Taillet, Phys. Rev. **A41**, 3307(1990).

[6] F. F. Chen, in "*Introduction to Plasma Physics*",(Plenum, New York, 1974),p. 96.

[7] H. Takeda, Master's thesis at Doshisha Univ., 1988.

[8] M. Nishiura, M. Sasao, and M. Bacal, J. Appl. Phys. **83**, 2944(1998).

Chapter 4

Theoretical analysis of plasma dynamics perturbed by photodetachment

4.1 Introduction

Plasma, which contains negative ions, has been studied in the fields such as astrophysics, negative ion source development, and divertor plasma physics for neuclear fusion. Laser photodetachment method assisted with Langmuir probe is considered to be most useful as a diagnostic tool of negative ions in plasma, and lead us to well understanding of production mechanisms of negative ions.

Photon energy of a laser higher than the electron affinity causes the laser photodetachment of Eq. (2.9); $A^- + h\nu \rightarrow A + e^-$. This reaction leads to a sudden increase of the electron density, δn_e, on the laser path in negative ions containing plasmas. When all the negative ions are destroyed, $\delta n_e/n_e$ corresponds to the ratio of the negative ion density to the electron density, n_-/n_e. Using this relation, negative ion densities of hydrogen in plasma were first measured by the use of a laser photodetachment assisted with a positive biased Langmuir probe in 1979[1, 2]. The time evolution of electron currents after photodetachment showed the slow recovery with the time scale of positive or negative ion transit time. The negative ion temperature could be obtained by means of the recovery time as well as two laser photodetachment method[3]. The consistency of both methods was verified experimentally. They have reported that the thermal velocity of negative ions is in rough agreement with the velocity of outgoing electrons. In order to understand this phenomenon, the kinetic equation coupled with the Poisson equation has been utilized by neglecting the electric field dependent terms[4]. They have developed the transport dynamics

theory, in which the laser irradiated region is filled with negative ions from the surrounded region and then the sudden increase of electrons inside the laser channel goes outward with the same charge counterflow. The analytic solution of the inward flow of negative ions toward the laser axis is given as follows; $n_-(r = 0, t) = n_{-0} \exp\left[-(R/v_{th}^- t)^2\right]$, where r is the location of the Langmuir probe from the center of the laser beam, R is the laser radius, v_{th}^- the thermal velocity of negative ions, and n_{-0} background negative ion density. From this result the recovery time of photodetached electron current τ_r has the following relation with the thermal velocity of negative ions; $\tau_r \propto R/v_{th}^-$. This ballistic model is valid only under the condition of early recovery time and small potential perturbation, and can not explain a spatial profile and overshoot in time evolution of photodetached electron current.

The ballistic model was extended to include the effects of the self-consistent electric field [5]. Friedland et al. have proposed the theory of the hybrid fluid-kinetic model, in which the motions of electrons and positive ions obey the fluid equation and those of negative ions are governed by the kinetic equation. The general formulations for negative ion density $n_-(r, t)$ and photodetached electron density $\delta n_e(r, t)$ are given in Ref.[5]. For actual applications, $n_-(r = 0, t)$ and $\delta n_e(r = 0, t)$ are demonstrated with using the smoothing functions for both slab and cylindrical geometry instead of a delta function. The time traces of photodetached electron current including an overshoot at $r = 0$ are shown numerically in their paper. It is found that the overshoot current with respect to the photodetached electron current depends on the ratio of electron temperature to positive ion temperature, T_e/T_+. They concluded the depletion of positive ions, which is arised from the difference of the thermal velocities between electrons and ions, causes the overshoot. Details are noted in the previous chapter.

As have been been shown in the previous chapter and in Ref. [6], the observed photodetachment currents are independent of the laser photon energies for photodetachment. The hybrid fluid-kinetic model is applied for the analysis of the measured ratios of the photodetachment current to the overshoot current in time traces of electron current at various T_e, and the reasonable $T_+ = 0.1$ eV is obtained.

Ivanov et al. pointed out the importance of the self-consistent electric field in case of the density ratio of negative ions to positive ions higher than 0.1 for the negative ion perturbation [7]. As another approach, they have also solved the dynamics for perturbed electrons in a planar geometry under the condition that $T_+ \sim T_e$ using the linearized Vlasov equation [8]. The solution for perturbed electrons agrees with those given by the hybrid fluid-kinetic model in the limit

$T_+ \to 0$.

It is important to analyze perturbed densities both inside and outside the laser beam in order to confirm the validity for the hybrid fluid-kinetic model. The perturbed profile contains rich information about the estimate of the negative ion density and other plasma parameters. However the analysis at $r > R$ still remains not to be understood physical pictures of laser photodetachment perturbation in plasmas, especially in experimental aspects. This may lead to the misunderstandings in analysis.

Now we are concerned with changes of electron density in both time and space due to photodetachment in a cylindrical geometry. In this chapter, we begin with introducing the hybrid fluid-kinetic model, and extend it to analyze the plasma response at $r \geq 0$ using the general solutions of $\delta n_e(r,t)$ and $\delta n_-(r,t)$ until the plasma recovers to the original condition. The results are compared with the typical experimental data in order to confirm the hybrid fluid-kinetic model.

4.2 Experimental configuration

The schematic diagrams of experimental setup and measurement system are noted in section 3.2 and the details are also shown in Figs. 3.1, 3.2, and 3.3. The discharge chamber is made of a stainless-steel vessel of 270 mm in length and 210 mm in diameter. Ten rows of ferrite magnets are attached on the cylindrical wall for the plasma confinement. Each end of the vessel has also four magnets. The vessel is biased at $\sim$ 100 V as an anode. The hydrogen plasma is produced by two tungsten filaments as cathodes.

The L-shaped Langmuir probe is installed into the plasma. The probe tip is made of a tungsten wire of 10 mm in length and ϕ 0.35 mm in diameter. The Nd-YAG laser was used for photodetachment. The laser beam diameter is limited to 4 mm using the aperture. The laser power was kept constant at the saturation region of the excess electron current due to photodetachment.

The produced dc plasma is uniform and unmagnetized in the central region of the vessel. Plasma parameters of $n_e = 10^{10} \sim 10^{11}$ cm^{-3}, $T_e = 0.5 \sim 3$ eV, and $n_-/n_e \sim 0.05$ are obtained from the probe $I - V$ characteristics and photodetachment measurement in Fig. 3.6. After photodetachment the typical Langmuir probe signals are shown in Figs. 2.3(a)$r = 0$ mm and 2.4(b)$r = 6$ and 8 mm. When the detachment of all electrons from H^- ions is induced by enough laser power, the relation of Eq. (2.11) [1]; $n_-/n_e = \Delta I/I_{dc}$, is used for determining the

n_-/n_e ratio.

The differences between the profiles of the probe signal located inside the laser beam and the outside one are studied in the subsequent sections.

4.3 Basic equation and model

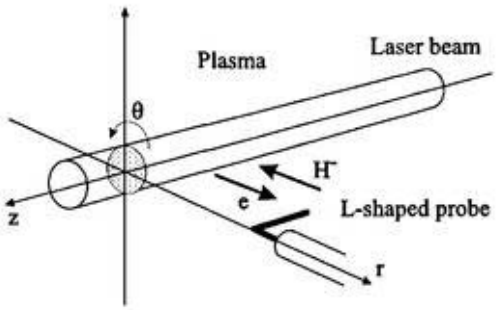

Figure 4.1: Illustration of the laser beam and the probe for a model calculation.

Although a plasma in a negative ion source usually contains various species; positive ions(H^+, H_2^+, H_3^+), negative ions(H^-), and electrons, the plasma considered here is assumed to consist of three species of charged particles; positive ions(H_3^+), electrons(e^-), and negative ions(H^-). The magnetic field can be ignored and the plasma is homogeneous in our case. When the plasma is irradiated with a laser beam, which destroys all the negative ions, electrons from negative ions increase suddenly due to the photodetachment reaction in its path, $r \leq R$. For $r > R$, all species are not disturbed by photodetachment at $t = 0$. The excess electrons in the laser irradiated region, $r \leq R$, do not feel anything initially, but the electrons near the edge($r \sim R$) feel the density gradient. The negative ions act on filling in the depleted region across the discontinuous edge. At the same time, excess electrons due to photodetachment moves outward in place of the negative ion flow. The perturbed plasma recovers to the initial condition with a time scale of R/v_{th}^-.

This plasma response does not include the negative ion production. The following rate equation can be used to estimate the production ratio of negative ions during the recovery.

$$dn_-/dt = n_e n_{H_2} \overline{\sigma v}(DA) - n_{-0} n_e \overline{\sigma v}(ii).$$

Integrating over t above equation,

$$n_- \approx \left(n_e n_{H_2} \overline{\sigma v}(DA) - n_{-0} n_e \overline{\sigma v}(ii)\right) \times t_r$$

$$\simeq \quad 10^8 \leq n_{-0} \ll n_{e0}.$$

Here the initial background electron density $n_{e0} = 10^{10}$ cm^{-3}, the vibrationally excited molecule density $n_{H_2} = 10^{13}$ cm^{-3}, $n_{-0} = 10^9$ cm^{-3}, $\overline{\sigma v}(DA) = 10^{-9}$ cm^{-3}/s, and $\overline{\sigma v}(ii) = 10^{-7}$ cm^{-3}/s, are used as parameters under a typical discharge condition. This means the effect on the production of negative ions can be ignored in the case of the single pulse photodetachment. It must take care in the case of the double pulse photodetachment at a large time scale. We may treat a collisionless scheme for plasma particles in the time scale less than a few times of that of recovery.

As shown in Fig. 4.1, a cylindrical geometry is employed for the analytical advantages and actual applications. The z direction coincides with the laser axis. The radial direction of the laser is chosen as r. The rotational direction is θ. Then the plasma must be infinite in length. The cylindrical probe does not disturb the plasma, and the sheath effects can be ignored.

With the foregoing in mind, an analytical model for a plasma response caused by photodetachment outside the laser beam is constructed. In case of a cold plasma, the continuity and momentum equations for positive ions become,

$$\frac{\partial(\delta n_+)}{\partial t} + n_{+0}\frac{(\delta v^+)}{\partial r} = 0, \tag{4.1}$$

$$M_+\frac{\partial(\delta v^+)}{\partial t} = -e\frac{\partial(\delta\phi)}{\partial r} - \frac{\gamma_i \kappa T_+}{n_{+0}}\frac{\partial(\delta n_+)}{\partial r}, \tag{4.2}$$

where M_+ indicates the mass of the positive ion, κ the Boltzmann constant, v the velocity of the particle, $\delta\phi$ the perturbed potential, γ_i the adiabatic constant for ions($\gamma_i = 3$), δ the perturbed quantity, the subscripts(e, -, +) the species of charged particles, and the subscript(0) the background density, respectively. Hereafter we apply the notations for mentioned parameters.

When the bulk and detached electrons are described by a Maxwellian distribution function, the field dependent electron density, δn_e, is linearlized by Boltzmann relation,

$$\delta n_e = n_{e0}\frac{e(\delta\phi)}{\kappa T_e}, \tag{4.3}$$

where n_{e0} is the background electron density, and T_e the electron temperature, respectively. The quasi-neutrality becomes an enough approximation in first order,

$$\delta n_+ = n_- - n_{-0} + n_e. \tag{4.4}$$

The motion of negative ions is dominated by the kinetic equation:

$$\frac{\partial f^-}{\partial t} + \boldsymbol{v}\cdot\frac{\partial f^-}{\partial \boldsymbol{r}} + \frac{e}{M_-}\left(\boldsymbol{E} + \frac{\boldsymbol{v}\times\boldsymbol{B}}{c}\right)\cdot\frac{\partial f^-}{\partial \boldsymbol{v}} = 0, \tag{4.5}$$

where f^- indicates the distribution function for negative ions. Since the nonlinear term would be negligible during the early time period and $\boldsymbol{B}$ in an unmagnetized plasma, Eq. (4.5) can be reduced to the simplified form,

$$\frac{\partial f^-}{\partial t} + \boldsymbol{v} \cdot \frac{\partial f^-}{\partial \boldsymbol{r}} = 0. \tag{4.6}$$

The variation of the negative ion density is given by

$$\Delta n_- \equiv n_- - n_{-0} = \int \left(f^- - f_0^-\right) d^3v, \tag{4.7}$$

with the initial distribution for negative ions, f_0^-.

Here we introduce a Laplace transform in time, and a Fourier transform in space with respect to a set of equations (4.1) $\sim$ (4.4), (4.6), and (4.7) in order to obtain $\delta\phi(k,\omega)$. The solution of the potential, $\delta\phi(r,t)$, is obtained by inverting the Laplace transform and the Fourier transform. The details of the calculations are noted in Ref.[5]. Assuming the ion acoustic velocity, C_s, would be comparable to the thermal velocity of negative ions, v_{th}^-, the final results of δn_e and δn_- are shown as follows;

for electrons,

$$\frac{\delta n_e(r,t)}{n_{-0}} = 2\int_0^{+\infty} \frac{[v_a^2 - (v_{th}^+)^2]\Psi(r, v_a t) - [v^2 - (v_{th}^+)^2]\Psi(r, vt)}{(\pi^{1/2} v_{th}^-)[v_a^2 - v^2]} e^{-(v/v_{th}^-)^2} dv, \tag{4.8}$$

with using the relation, $v_a^2 = (v_{th}^+)^2 + \kappa T_e/M = (v_{th}^+)^2 + (v_{th}^-)^2$. Then we assumed $\kappa T_e/M = v_{th}^-$. This assumption is reasonable for the experimental results given in Fig. 3.8, which show the ion acoustic velocity for H_3^+ is very close to v_{th}^-, and thus leads to the condition of $T_e/T_- = 24/\pi$.

For negative ions,

$$\frac{\delta n_-(r,t)}{n_{-0}} = -\frac{2}{(\pi^{1/2} v_{th}^-)} \int_0^{\infty} \Psi(r, vt) e^{-(v/v_{th}^-)^2} dv. \tag{4.9}$$

The function $\Psi(r,a)$ in Eqs. (4.8) and (4.9), which includes the integration of the Bessel function, takes the following form,

$$\Psi(r,a) = \int_0^{\infty} r' dr' \int_0^{\infty} k dk \left[\frac{\Delta(r')}{n_{-0}}\right] \cos(ka) J_0(kr) J_0(kr'), \tag{4.10}$$

where,

$$\frac{\Delta(r')}{n_{-0}} = \begin{cases} 1, & \text{if } |r'| \le R, \\ 0, & \text{if } |r'| > R. \end{cases} \tag{4.11}$$

The step function $\Delta(r')$ is used to represent the initial distribution for excess electrons. This form generally depends on the profile of the laser beam naturally, but it is reasonable to adopt

Eq. (4.11) for our conditions, because we cut the tail of a gaussian beam to make the boundary of the laser beam sharp. In order to proceed the integration, Eq. (4.10) is transformed into

$$\Psi(r,a) = \int_0^\infty R\cos(ka)J_0(kr)J_1(kR)dk, \tag{4.12}$$

using Bessel functions of the zero and the first kind.

Friedland et al. provided the function $\Psi(r=0,a)$ with the help of a smoothing function corresponding to the step function, $\Delta(r')$. Then Eq. (4.10) has a simple form:

$$\Psi(0,a) = \int_0^\infty R\cos(ka)J_1(kR)dk. \tag{4.13}$$

This integration gives the analytical solution. Thus

$$\Psi(0,a) = \begin{cases} -1 & , \quad r \le R; \\ \\ \left[(a/R)^2-1\right]^{-\frac{1}{2}}\left[(a/R)+\left[(a/R)^2-1\right]\right]^{-1} & , \quad a > R. \end{cases} \tag{4.14}$$

In practice, Friedland et al. used the function with continuity at $a = R$ such as Eq. (4.14)[1], instead of Eq. (4.12).

Substituting the function $\Psi(r,a)$ of Eq. (4.12) into Eq. (4.9), the integration over v can be carried out [10],

$$\frac{\delta n_-(r,t)}{n_{-0}} = -\frac{2}{(\pi^{1/2}v_{th}^-)}\int_0^\infty J_0(kr)J_1(kR)e^{-\left(kt v_{th}^-/2\right)^2}d(kR). \tag{4.15}$$

This remained integration satisfies the form of the hyper geometric function, if at $r/R = 1$. Equation (4.15) at $r = 0$ corresponds to Eq. (A.3) in the ballistic theory(see Appendix A).

For the sake of convenience and simplicity, we introduce dimensionless quantities:

$$\begin{aligned} x &= \sqrt{\frac{M}{\kappa T_e}}v = \frac{v}{v_{th}^-}; \\ \tau &= \frac{v_{th}^- t}{R}; \\ \alpha &= \sqrt{\frac{\gamma T_+}{T_e}}; \\ \eta &= \frac{r}{R}; \\ \xi &= kR. \end{aligned}$$

The quantities x and τ may be thought of as the velocity of charged particles in a plasma and the time after the photodetachment occurred. α denotes the ratio of positive ion temperature to

[1] Eq. (36) in Ref. [2]

electron temperature. η is the normalized distance from the center of the laser beam to the radial direction in the cylindrical coordinate. Using these quantities, Eq. (4.8) for the perturbation of the electron density becomes:

$$\frac{\delta n_e(\eta,\tau)}{n_{-0}} = \frac{2}{\sqrt{\pi}}\int_0^\infty \frac{\Psi(\eta,\sqrt{1+\alpha^2}\,\tau) - (x^2-\alpha^2)\Psi(\eta,x\tau)}{1+\alpha^2-x^2} e^{-x^2} dx, \tag{4.16}$$

where:

$$\Psi(\eta,x\tau) = \int_0^\infty \cos(x\tau\xi) J_0(\eta\xi) J_1(\xi) d\xi. \tag{4.17}$$

Equation (4.9) for the negative ion density becomes:

$$\frac{\delta n_-(\eta,\tau)}{n_{-0}} = \int_0^\infty J_0(\eta\xi) J_1(\xi) e^{-\left(\frac{\tau\xi}{2}\right)^2} d\xi. \tag{4.18}$$

Both Eqs. (4.16) and (4.18), which represent the perturbations of the electron density and the negative ion density, are calculated numerically.

4.4 Results and discussion

4.4.1 The perturbed potential at $\eta = 0$

Figure 4.2 shows the time evolutions of typical probe signal and calculated signals after photodetachment at $\eta = 0$ in the cases of (a)T_e = 0.86 eV and (b)T_e = 0.55 eV. The hydrogen gas pressure, P_g, is adjusted to change the electron temperature with keeping the discharge current. The ordinate indicates the perturbed electron density normalized by the maximum. The abscissa is the time normalized by the recovery time, of which the perturbed density becomes the original density first after photodetachment. The electron temperatures and densities are obtained from the results of the probe $I - V$ characteristic. The observed δn_e has a slow rise time after photodetachment. This time lag is about 20 ns, which is much larger than the order of the plasma oscillation time, $1/f_p$. The time scale is considered to be of the order of the propagation time of the perturbed electrons through the probe sheath with an ion acoustic velocity, $\lambda_D/C_s = \lambda_D/(R/t_r) = 0.1\times10^{-3}/(2\times10^{-3}/400\times10^{-9}) = 20$ ns. This information is important and useful for the analysis of sheath formation. However the additional explanations about the rise time are needed, because the time lag tends to be inversely proportional to the ion acoustic velocity, but it is independent of the Debye length.

In the region of larger τ, the observed photodetachment current approaches zero with a slow oscillation. The calculated δn_e also behaves similarly.

The experimental trace of δn_e is in good agreement with that calculated at both $\alpha = 0.59$ and 0.74. As α decreases gradually, the overshoot of the electron density becomes larger. This means that the growth of the self-consistent electric field becomes larger, due to the difference between the electron temperature and the positive ion temperature.

The measured ratios of the overshoot to the photodetachment current $I_{ov}/\Delta I$ are plotted as a function of the electron temperature for various discharge currents, as shown in Fig. 4.3. Four lines are the calculated ratios of $\alpha = 0.74, 0.59, 0.5, 0.4$, and 0.25 as a parameter of T_+. The hydrogen gas pressure is adjusted to change the electron temperature. When the discharge current kept constant, the measured $I_{ov}/\Delta I$ exists on the same calculated line. From the results, the positive ion temperature can be determined. Even if T_e is varied over a range of 0.5 to 2.5 eV, T_+ does not change, if the discharge current is kept constant. This result is reasonable, because the positive ions are produced by collisions between high energy electrons and hydrogen molecules. On the other hand, the negative ion temperature increases as the electron temperature goes up for the reason that the negative ion is produced by dissociative electron attachment from viblationally excited molecules of H_2.

4.4.2 Propagation of perturbed potential

Devynck et al.[3] and Nishiura et al.[6] have already reported the outward propagation of the perturbed potential experimentally, compared with the ion acoustic velocity. Then we confirmed that the peak of perturbed potential moves outward with the ion acoustic velocity, while it does not attenuate as a ballistic locus corresponding to $1/r$. The general characteristics of charged particle propagation are needed to be understood substantially by the time and spatial pictures.

For the determination of the effective laser radius, the time evolutions of the perturbed electron density are shown in Fig. 4.4. The Langmuir probe is located at (a)$r = 4$ mm, (b)$r = 5$ mm, and (c)$r = 6$ mm, respectively. The ordinate indicates the perturbed electron density normalized by that at $r = 0$ mm. Although the actual laser beam radius should be 2.0 mm, r is normalized by $R = 2.5$ mm because of the density gradient at the laser boundary. The calculated potentials at $\eta = 1.6$, 2, and 2.4 are also plotted in these figures. The calculated peaks of perturbed electron density coincide with the observed peaks at each case. However the profile of the laser beam may cause the difference of the signal broadening between the observed data and the calculation. The precision of the Langmuir probe would be poor in space to an extent of several Debye lengths.

4.4.3 Two-dimensional view of perturbed density

Figure 4.5 shows the recovery of the negative ion density calculated using Eq. (4.18) from τ =0 to 3.0. The vacant valley inside the laser channel is filled with the negative ions gradually from the boundary of the laser beam path. It is clear that the recovery of the negative ion density does not depend on α from Eq. (4.18). The effect of α must be considered in a strict sense, because the positive ions influence on the self-consistent electric field, even if it may be a small perturbation. The graphs in Fig. 4.6 are shown for comparisons in the perturbed electron densities. Although the laser radius is limited to $\eta = 0.8(r = 2$ mm), the gradient of the actual electron density starts at $\eta = 0.7$ and decreases exponentially to about 2.0. This reason would be also due to the spatial resolution of the Langmuir probe mentioned in the previous section. Until $\tau = 0.6$, the perturbed potential at $\eta < 1$ seems to be hollowed out, while the perturbed one at $\eta > 1$ is pushed out outward with the symmetry near $\eta = 1$. When $\tau = 1.1$, the overshoot emerges at $\eta = 0$. The calculated values of less than zero tend to become larger than the measured values. The discrepancy would be in a calculation error of numerical integration.

4.4.4 Determination of negative ion density from signal measured at $\eta \neq 0$

A peak of potential pulse perturbed by photodetachment propagates outward with the ion acoustic velocity, as shown in Fig. 4.6. If we can regard a laser beam as a line at a position far away from the laser beam, the peak of the potential pulse would dump in reverse proportion to the distance from the center of the laser beam. Since the absolute values of the potential peaks, however, depend on the ratio of T_e/T_+, the calculation is needed to determine $n_-(0,0)$ from the measurement at $\eta > 0$. The measured peak of the potential pulse is compared with the calculation in Fig. 4.7. Experimental data agree well with the results of the calculations. Therefore if T_e/T_+ can be obtained from the analysis of a signal, it is found $\delta n_e(0,0)$ can be determined precisely. It leads us to determining the negative ion density at $\eta = 0$ from a measurement of a perturbed potential at $\eta > 0$.

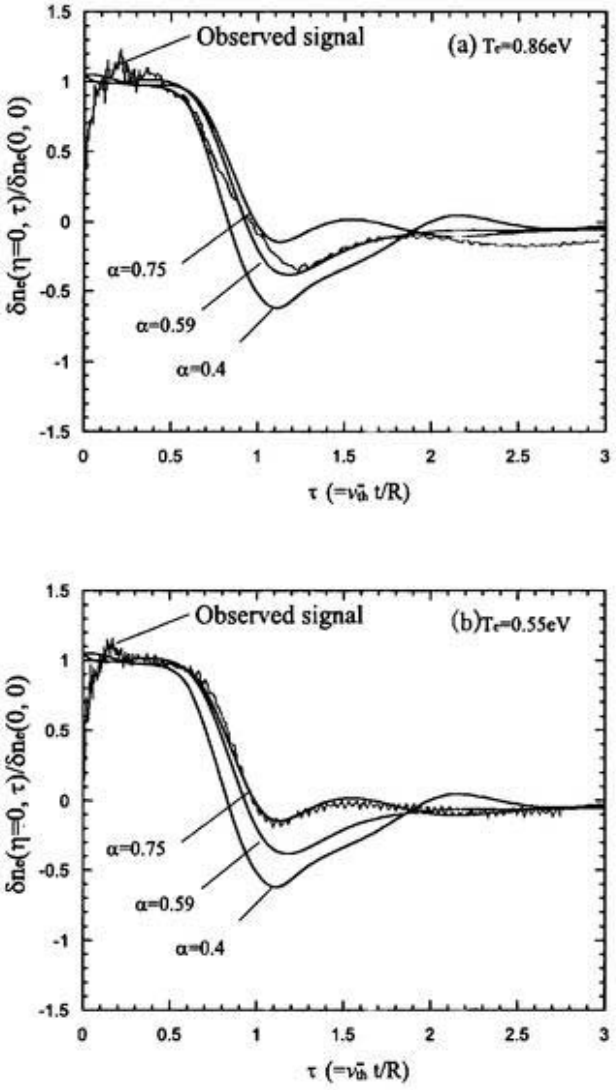

Figure 4.2: The observed signal and the calculated traces at $\eta = 0$ (laser beam center). The photodetachment signal is measured in the cases of (a) $\alpha = 0.59$ under the conditions: $P_g = 2.2\text{mTorr}, n_-/n_e = 0.01$, $n_e = 7 \times 10^{10}\text{cm}^{-3}$, $T_e = 0.86$ eV, and $T_+ = 0.1$, and (b) $\alpha = 0.74$ under the conditions: $P_g = 2.2\text{mTorr}, n_-/n_e = 0.0055$, $n_e = 8.7 \times 10^{10}\text{cm}^{-3}$, $T_e = 0.55$ eV, and $T_+ = 0.1$. The observed signals of $\alpha = 0.59$ and 0.74 agree with the calculations.

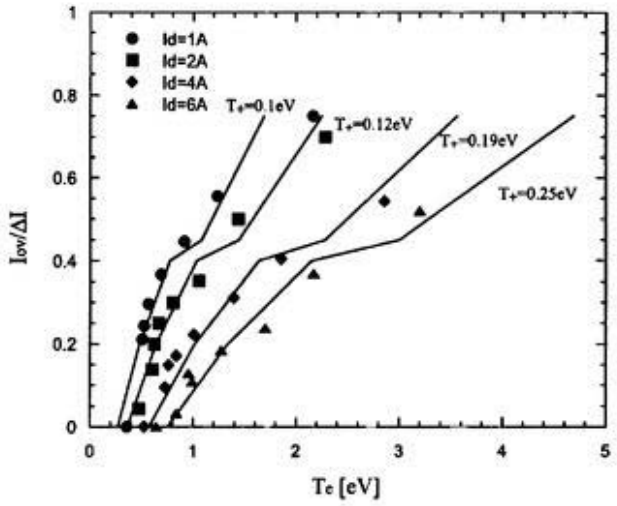

Figure 4.3: Dependence of the overshoot signal on the electron temperature for various discharge currents of 1, 2, 4 and 6 A. The symbols indicate the measured data. The four lines indicate the calculated values of the overshoot signal, and are fit to coincide with the measured data using the parameters of T_+. The electron temperatures were changed by the adjustment of the hydrogen gas pressure.

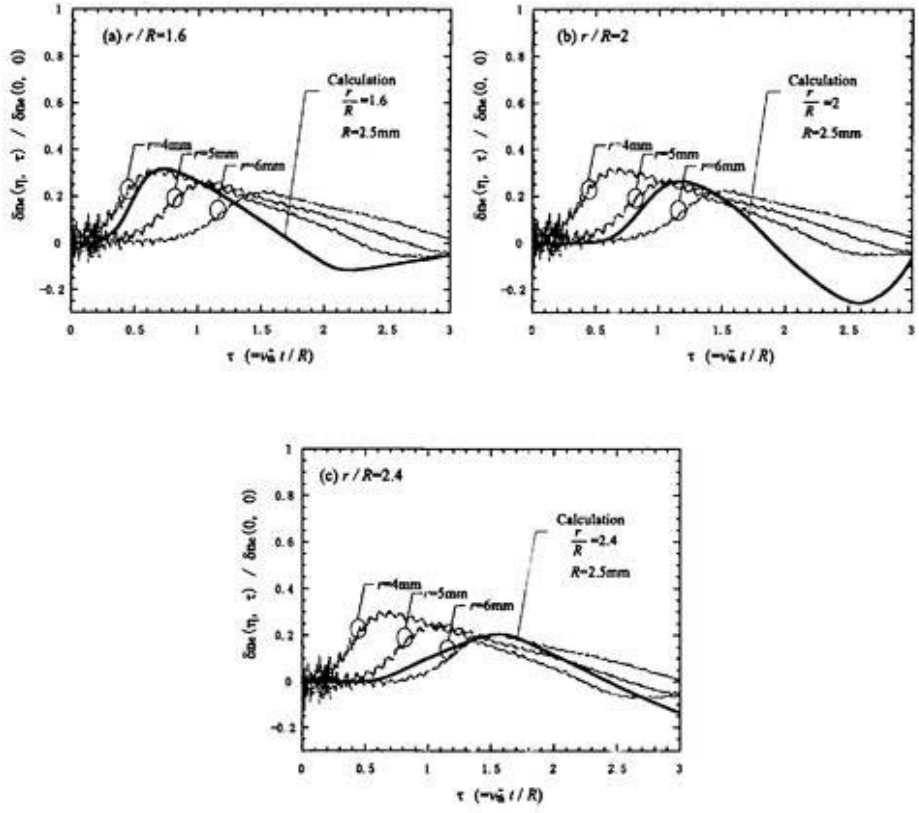

Figure 4.4: Comparison between the observed signals and the calculated traces(thick line) under the conditions that $\alpha = 0.59$ and $R = 2.5$ mm. (a)$r/R = 1.6$, (b)2.0, and (c)2.4. Experimental data are obtained under the conditions where $n_-/n_e = 0.01$, $n_e = 7 \times 10^{10}\mathrm{cm}^{-3}$, and $T_e = 0.86$ eV in a hydrogen plasma. The peak position of observed signal agrees with the calculations at each probe position.

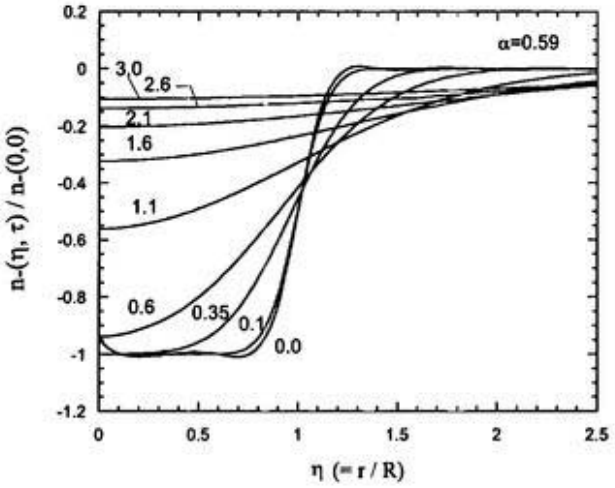

Figure 4.5: Calculations of spatiotemporal transition of perturbed densities for negative ions. $\alpha = 0.59$ and $R = 2.5$ mm are used for calculations. The numbers in the figure indicate the time τ, after the photodetachment. τ is normalized by $(v_{th}^{-}/R)^{-1}$, and therefore $\tau = v_{th}^{-}t/R$. The perturbed electron density moves from left to right.

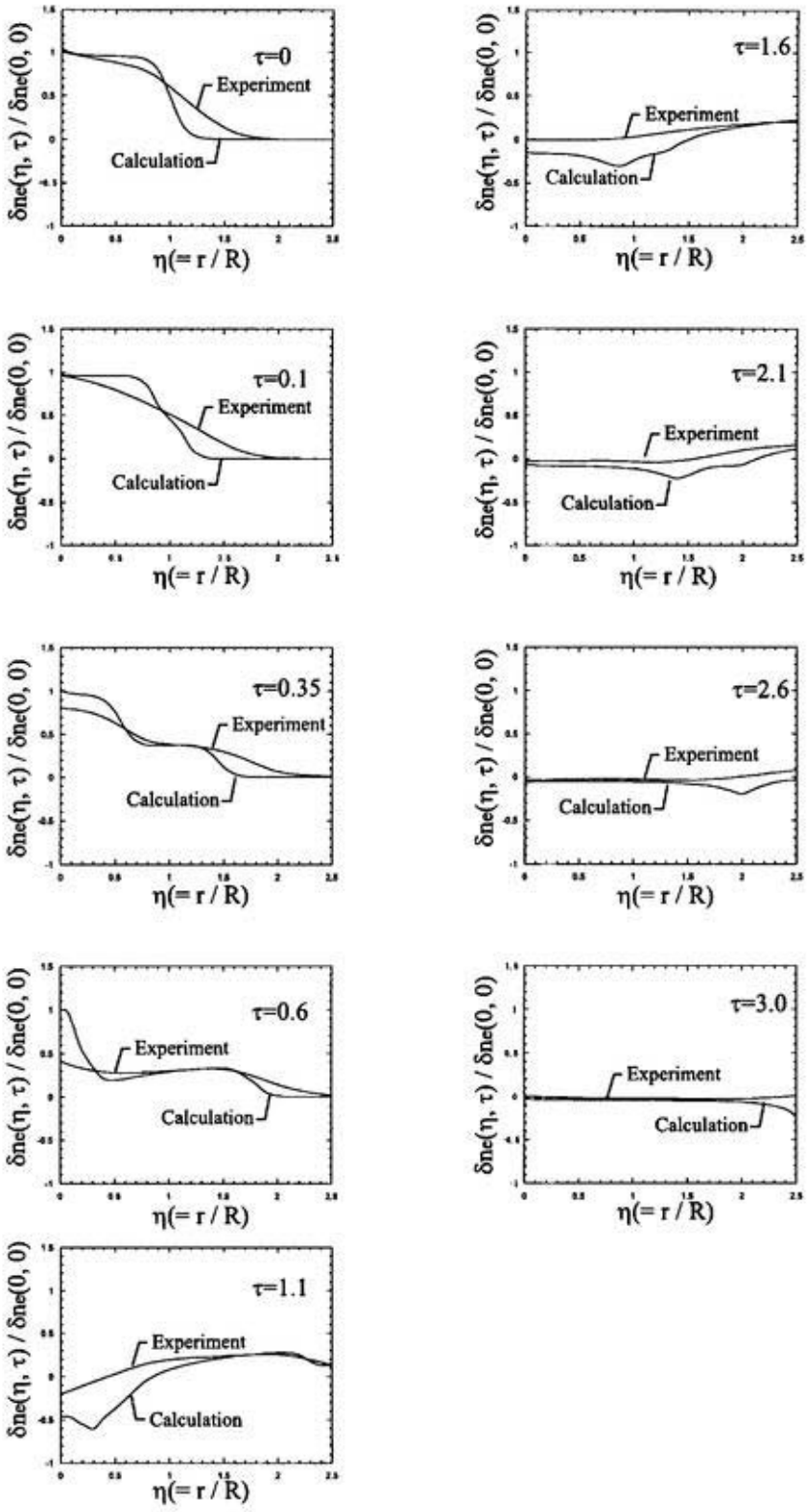

Figure 4.6: Comparison of spatiotemporal transition changes of perturbed electron densities between the observed data and the calculations at $\tau = 0, 0.1, \ldots, 3.0$ under the conditions that $\alpha = 0.59$ and $R = 2.5$ mm. Experimental data for electrons are obtained under the condition where $n_-/n_e = 0.01$, $n_e = 7 \times 10^{10}\text{cm}^{-3}$, and $T_e = 0.86$ eV in a hydrogen plasma. The perturbed electron density moves from left to right.

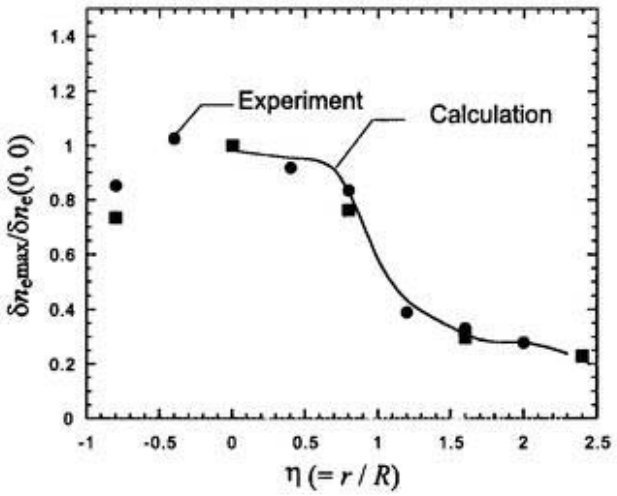

Figure 4.7: Change of maximum of the perturbed electron density at each probe position. The symbols indicate the observed peak value of probe signal. The data are obtained by moving the probe position with increasing η(circles) and with decreasing η(squares). The thick line is the calculated values of perturbed electron densities in the case of $\alpha = 0.59$ and $R = 2.5$ mm.

Bibliography

[1] M. Bacal and G. W. Hamilton, Phys. Rev. Lett. **42**, 1538(1979).

[2] M. Bacal, G. W. Hamilton, A. M. Bruneteau, and H. J. Doucet, Rev. Sci. Instrum. **50**, 719(1979).

[3] P. Devynck, J. Auvray, M. Bacal, P. Berlemont, J. Bruneteau, R. Leroy, and R. A. Stern, Rev. Sci. Instrum. **60**, 2873(1989).

[4] R. A. Stern, P. Devynck, M. Bacal, P. Berlemont, and F. Hillion, Phys. Rev. A**41**, 3307(1990).

[5] L. Friedland, C. I. Ciubotariu and M. Bacal, Phys. Rev. E**49**, 4353(1994).

[6] M. Nishiura, M. Sasao and M. Bacal, J. Appl. Phys. **83**, 2944(1998).

[7] A. A. Ivanov, L. I. Elizarov, M. Bacal, A. B. Sionov, Phys. Rev. E 52, 669(1995).

[8] A. A. Ivanov, A. B. Sionov, C. I. Ciubotariu, M. Bacal, Fizika Plasmy, No. 8, (1998).

[9] D. A. Skinner and C. Courteille, Phys. Plasma. **1**, 2785(1994).

[10] I. S. Gradshteyn and I. M. Ryzhik *"Table of integrals, series, and products"* (Academic Press, New York, 1980).

Part II

Applications of negative ion diagnostics

Chapter 5

Plasma characteristics of cesium seeding in the driver region

5.1 Introduction

In order to extract a high current H^- ion beam from an ion source, cesium injection has been considered as an effective method experimentally. However the enhancement mechanism of H^- production in an ion source due to cesium injection is still not well understood. Bacal et al. [1] have investigated the enhancement of H^- density by diagnosing the Cs seeded plasma in the center of the extraction region using a photodetachment method associated with a Langmuir probe to obtain the H^- density and temperature. The increase of H^- density/electron density ratio is observed by the addition of Cs. In a tandem H^- ion source, vibrationally excited molecules of hydrogen are produced in the driver region, where high energy electrons are present. Cs injection into the source should affect plasma parameters of this region as well as the extraction region. Therefore, we have investigated the plasma parameters of the driver. In a driver region, the plasma parameters, which include H^- density, are investigated in a cesium injection case.

5.2 Experimental setup and method

A. Experimental setup

Figure 5.1 illustrates the arrangement of this experiment. The details of the discharge chamber are explained in chapter 3. Two instruments are newly installed to the ion source. One is a cesium oven with heaters and thermocouples on the end plate. The other is an optical fiber, connected to a view port, for spectroscopic measurement. The discharge chamber is a stainless-steel vessel of 270 mm in length and 210 mm in diameter. The side wall of the vessel is surrounded by ten rows

of ferrite magnets arranged to produce a cusp magnetic field, which is about 300 Gauss on the surface of the wall and a few Gauss at the center of the vessel. The H^- density and the electron density are measured at the field free region. Four ferrite magnets on the end plate are used for plasma confinement. Two Tungsten filaments, which are attached to the current feedthroughs on the end plate, generate primary electrons. Hydrogen gas is admitted into the ion source through a port in the center of the end plate. The gas pressure is always monitored by using an ionization gauge.

A cylindrical Langmuir probe is installed perpendicularly to the laser beam. The tip of the L-shaped probe, which is made of a tungsten wire, is 10 mm in length and 0.35 mm in diameter.

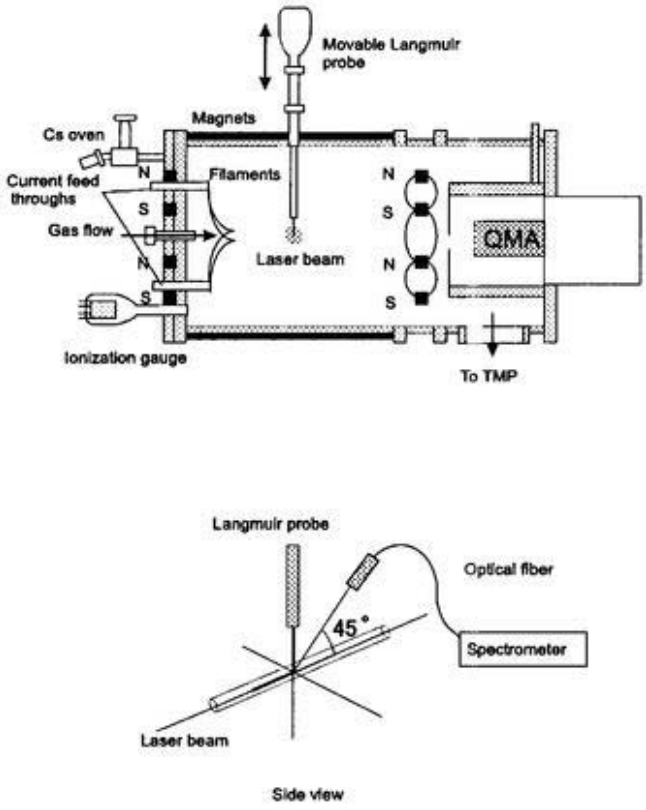

Figure 5.1: Illustrations of the multicusp ion source with the cesium oven and spectrometer.

B. Cesium operation and detection

Metallic cesium of 1 g is put into a Cs oven. Prior to the experiment the Cs oven is heated to 300 °C with the valve closed. After that the oven is cooled to a room temperature. The

stainless steel tube to introduce the cesium into the discharge chamber is kept at about 300 °C. After a while, the valve is opened. The oven is heated up to 200 °C gradually. We monitor the intensities of Cs and H_α spectra to estimate the amount of Cs in an H_2 dc discharge by use of a spectroscope. A spectrometer(HAMAMATSU, PMA-11) has been used in order to detect the cesium spectrum D-lines(852nm, 892nm) [2] in an H_2 discharge. Figure 5.2 shows an example of spectrum lines, $H_{\alpha,\beta,\gamma}$ (656 nm, 486 nm and 434 nm) and Cs, in an H_2 discharge. The intensity of the base line is attributed to the filament emission. The intensity of Cs is greatly influenced by the wall temperature of the discharge chamber. Throughout the experiment, the wall temperature is maintained by a dc discharge.

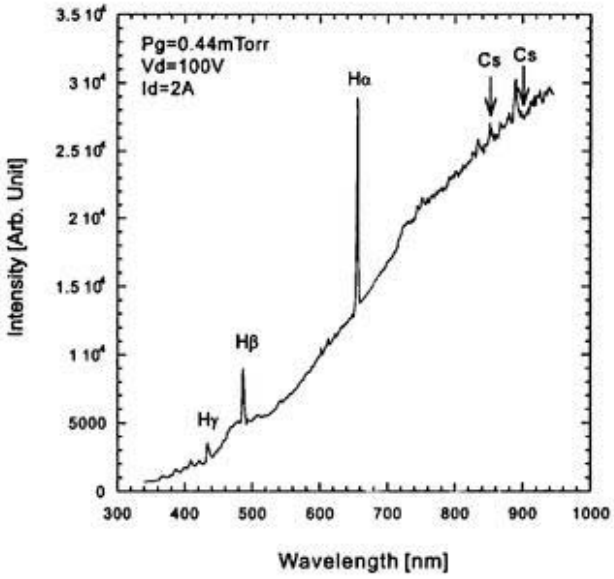

Figure 5.2: Optical emission intensity in the ion source in a Cs seeded case.

The residual gases(for example, H_2O and O_2) are checked by a quadrupole mass analyzer(QMA, Balzaers Prisma, QMS200F) installed in the downstream of the discharge chamber. In a Cs seeded case, the Cs spectrum can not be detected by QMA in an H_2 discharge. After the discharge is turned off, the Cs spectrum can be detected as a residual gas at the background vacuum of 4×10^{-7} Torr.

5.3 Results and discussion

A. Measurement of the electron density n_e and the H^- density n_-

In a cesium seeded case, it is found that the probe $I-V$ characteristics are influenced by the adsorption of the cesium on the probe surface, as shown in Fig. 5.3. When the probe is contaminated by Cs, the plasma potential appears to shift lower than that without cleaning. After the probe surface, biased positively with respect to the plasma potential, is heated by the probe electron current, the probe voltage is swept quickly to the negative direction to minimize the effect of cesium contamination on the probe surface. Figure 5.4 shows the comparison of typical probe $I-V$ characteristics between with Cs and without Cs. Each arrow in the graph denotes the plasma potential. The curve in the cesium seeded case shifts in the positive direction by 0.4 V. The high energy tail due to fast electrons appears as the H_2 pressure increases. At the lower H_2 pressure the distinction between the high energy electrons and the bulk energy electrons is difficult. Since the density of high energy electrons is lower than that of bulk electrons, the high energy component is neglected. From the probe $I-V$ characteristics we obtain the electron density, n_e, the electron temperature, T_e, and the plasma space potential, V_s, respectively. Then the H^- density, n_-, is determined by measuring the ratio of photodetachment current to the electron current, $\Delta I/I_{dc}$ at 15 V of the probe power supply.

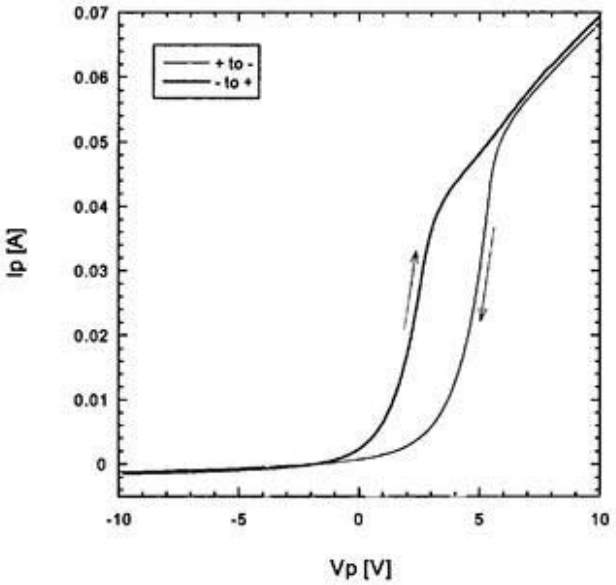

Figure 5.3: Characteristics of probe $I-V$ traces in a Cs seeded case at the pressure of 2.2 mTorr and $I_d = 2$ A. Arrows in the figure indicate the sweeping directions of the probe power supply.

Figure 5.5 shows the dependence of n_e and n_- on H_2 gas pressure in the pure volume case and the Cs seeded case. Present results do not show an increase of the H^- density, although the

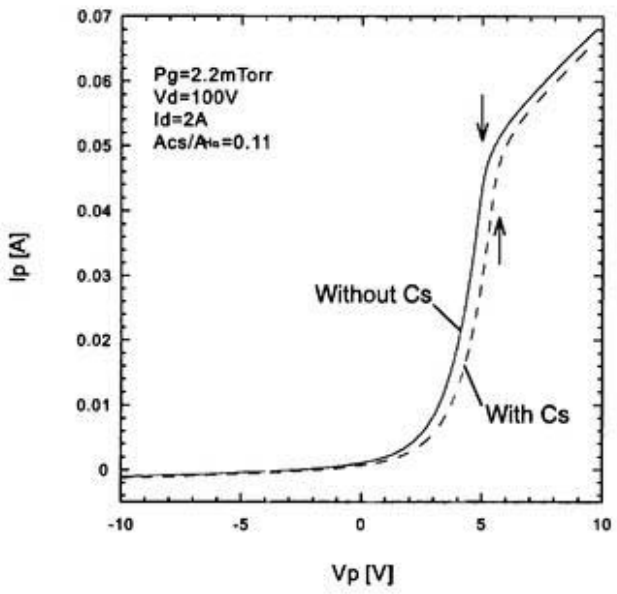

Figure 5.4: Characteristics of probe $I-V$ traces in a pure H_2 and a Cs seeded case.

cesium is introduced into the ion source. Both H_α intensity, A_{H_α}, and cesium D-line(852nm) intensity, A_{Cs}, are also measured simultaneously, as shown in Fig. 5.6. Since the baseline is considered as the continuum line from the filaments, the baseline fitted linearly is taken away from the raw signal in order to obtain A_{H_α} and A_{Cs}. As the H_2 gas pressure changes in the range from 0.44 to 18 mTorr, the intensity of Cs(852nm) decreases gradually. As the H_2 gas pressure is increased, the ratio of A_{Cs}/A_{H_α} is decreased from 0.6 to 0.01. Figure 5.7 shows the dependence of electron temperature, T_e, H^- temperature, T_-, and plasma space potential, V_s, on the H_2 gas pressure in a pure volume and in a plasma with Cs. From the results of T_e, the electron temperature did not decrease in the Cs seeded case. The enhancement of the n_-/n_e ratio and n_- is observed only at the lowest H_2 gas pressure of 0.44 mTorr. The plasma space potential becomes more positive by the cesium seeding.

B. Measurement of the H^- temperature T_- and the overshoot signal

The H^- temperature can be obtained by the photodetachment [6, 7]. Here we use Eq. (6) in ref. [6] to calculate the H^- temperature. In Fig. 5.7, T_- in the Cs seeded case tends to be lower than that in the pure H_2 case, regardless of the bulk electron temperature, T_e, which influences the dissociative attachment reaction rate.

Friedland et al. [8] have carried out the simulation of the time evolution of photodetachment

signal, $\Delta I - t$, in a plasma including H_3^+ ions, electrons and H^- ions. Their calculation shows the dependence of the overshoot signal on $\sqrt{T_+/T_e}$. In the pure H_2 case we applied their results to our experimental results in order to estimate T_+ [9]. By using the same manner figure 5.8 shows the dependence of $I_{ov}/\Delta I$ on T_e, where I_{ov} is the amplitude of the overshoot and ΔI is the photodetachment current in the probe signal. From two fitting lines to the measured data, the positive ion temperature is found to be between $T_+ = 0.12$ eV and 0.14 eV. An obvious change of $I_{ov}/\Delta I$ is not seen with the Cs introduction.

C. Dependence of n_-/n_e on A_{Cs}/A_{H_α}

The influence of Cs on the H^- volume production is investigated at 2.2 mTorr, as is shown in Fig. 5.9. The intensity of Cs is controlled by changing the wall temperature, while the H_α intensity is kept constant. The n_-/n_e ratios are different from the above experiment because the shape of the discharge filaments is different. The variation of the n_-/n_e ratio is small in spite of the change of the A_{Cs}/A_{H_α} ratio more than one order of magnitude.

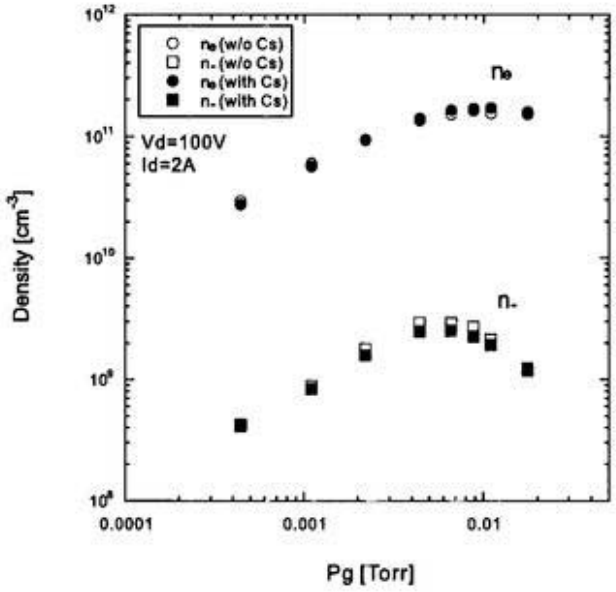

Figure 5.5: Dependence of electron and H^- density on H_2 gas pressure in a pure H_2 and a Cs seeded case. The discharge current I_d is 2 A.

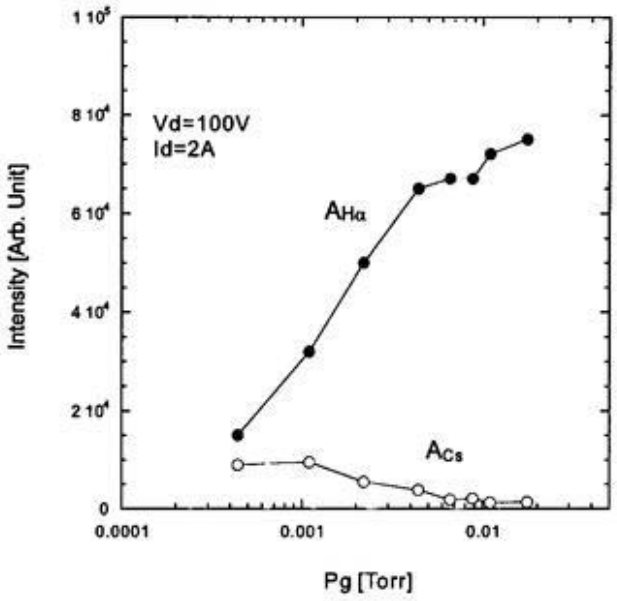

Figure 5.6: Dependence of n_-/n_e on the ratio of Cs intensity to H_α intensity, A_{Cs}/A_{H_α}, at the pressure of 2.2 mTorr.

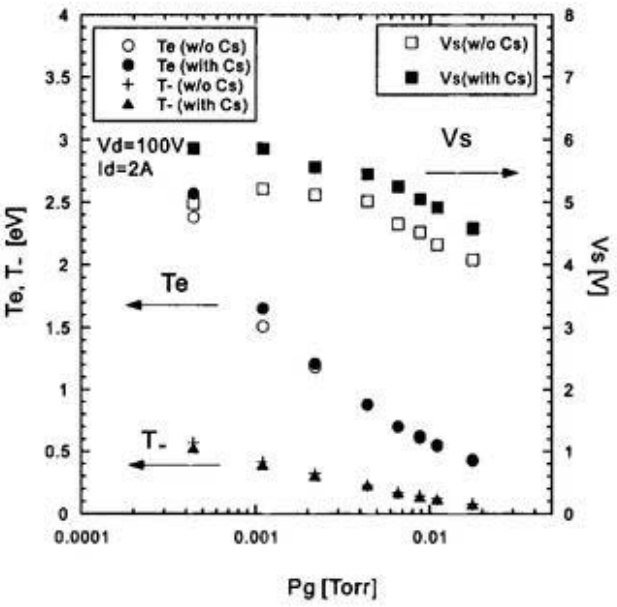

Figure 5.7: Dependence of T_e, T_-, and V_s on H_2 gas pressure in a pure H_2 and a Cs seeded case.

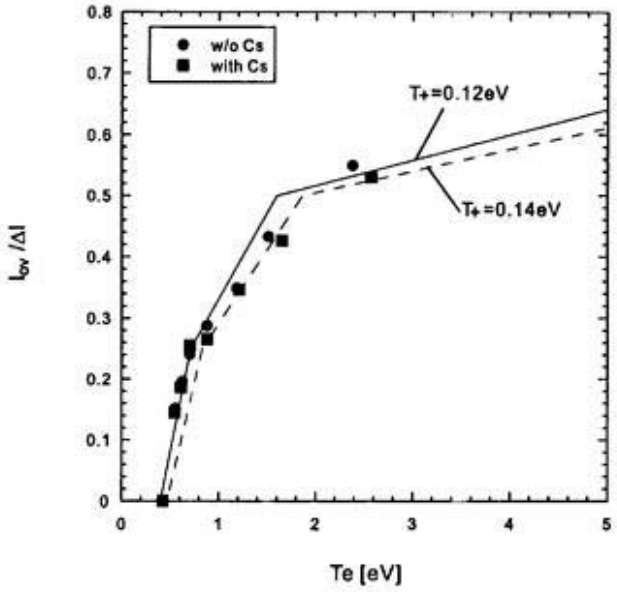

Figure 5.8: Variation of the overshoot/photodetachment signal ratio, $I_{ov}/\delta I$, with T_e. Broken line and solid line are the calculation results of Friedland et al. for $T_+ = 0.14$ and 0.12 eV. The positive ion temperatures are obtained by fitting our data to their calculations.

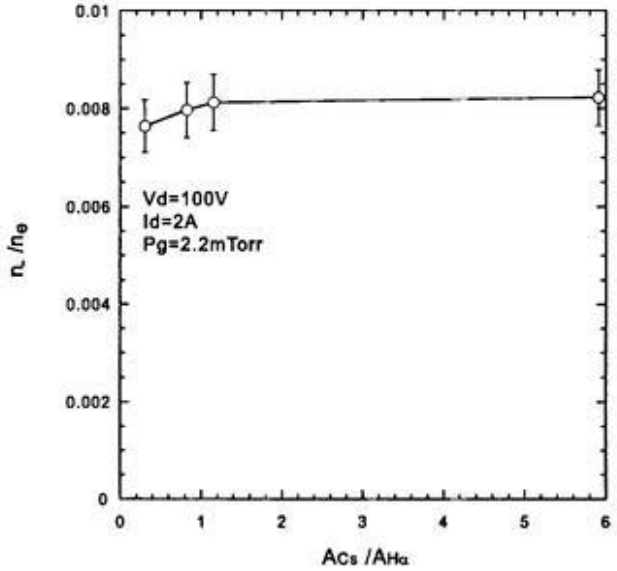

Figure 5.9: Dependence of n_-/n_e on the ratio of Cs intensity to H_α intensity, A_{Cs}/A_{H_α}, at the pressure of 2.2 mTorr.

Bibliography

[1] M. Bacal, C. Michaut, L. I. Elizarov, and F. El Balghiti, Rev. Sci. Instrum. **67**, 1138(1996).

[2] G. H. Harrison, MIT Wavelength Tables, MIT Press, Cambridge (1969).

[3] S. R. Walther, K. N. Leung, and W. B. Kunkel, J. Appl. Phys. **64**, 3424(1988).

[4] Y. Okumura, Y. Fujiwara, A. Honda, T. Inoue, M. Kuriyama, K. Miyamoto, N. Miyamoto, K. Mogaki, A. Nagase, Y. Ohara, K. Usui, and K. Watanabe, Rev. Sci. Instrum. **67**, 1018(1996).

[5] Y. Belchenko, C Jacquot, J. Pamela, and D. Riz, Rev. Sci. Instrum. **67**, 1033(1996).

[6] P. Devynck, J. Auvray, M. Bacal, P. Berlemont, J. Bruneteau, R. Leroy, and R. A. Stern, Rev. Sci. Instrum. **60**, 2873(1989).

[7] R. A. Stern, P. Devynck, M. Bacal, P. Berlemont, and F. Hillion, Phys. Rev. **A41**, 3307(1990).

[8] L. Friedland, C. I. Ciubotariu and M. Bacal, Phys. Rev. **E49**, 4353(1994).

[9] M. Nishiura, M. Sasao and M. Bacal, J. Appl. Phys. **83**, 2944(1998).

Chapter 6

Plasma Characteristics of alkali metal vapor seeding in the extraction region

6.1 Introduction

A negative ion source of volume production type can generate an intense beam efficiently and is useful for these applications. This type of ion source is generally divided into two regions by a magnetic filter field. The first region is called the driver region, and the second region is the extraction region. The former is the production region of vibrationally excited molecules. The latter is that of H^- ions formed by a dissociative electron attachment reaction. In this region vibrationally excited molecules, $H_2(v'')$, produced by collision with fast electrons in the driver region, encounter slow electrons in a low temperature plasma; [1, 2]

$$e + H_2(X^1\Sigma_g^+, v) \rightarrow H^- + H. \tag{6.1}$$

In order to extract the higher beam current at the optimum configuration, the addition of cesium has been useful method [3]. Nowadays cesium seeding has been widely used as a high current H^- beam for neutral beam injector, NBI, of fusion devices, for example, in JT-60U [4], and LHD [5]. It has been reported that the beam intensity of H^- tends to be improved especially at higher discharge power due to the cesium seeding. The possible reason of the H^- enhancement would be the surface production of H^- on the plasma electrode, where the cesium adsorption on the electrode causes the work function reduction on the surface, then the following processes may occur.

$$H^+ + 2e_{surface} \rightarrow H^- \text{ [6, 7, 8]} \tag{6.2}$$

$$H^0 + e_{surface} \rightarrow H^- \text{ [8, 9, 10, 11]} \tag{6.3}$$

Shinto et al. [12] have investigated the relation between the work functions of the cesium adsorbed molybdenum surface and the extracted H^- beam currents using the photoelectron emission method assisted with a laser light. Employing the probability for the surface production of H^- on a wall of an ion source, P_{cs}, Fukumasa et al. have solved the numerical balance equations in a steady state hydrogen plasma [13]. Their result shows a good agreement in the dependence of plasma parameters on hydrogen gas pressure. Apart from the surface process, other possibilities have been still remained in the H^- enhancement on the volume process. One is the electron cooling [2] due to the collision with cesium, another is the H^- production from CsH^- [14, 15];

$$CsH^- \rightarrow Cs + H^-. \tag{6.4}$$

In addition to these reactions Peterson [16] suggested the production of $H_2(v'')$ by $H_3^+ + Cs$ charge transfer as follows;

$$H_3^+ + Cs \rightarrow H_3^* + H + Cs^+. \tag{6.5}$$

Another possible process is the increase of $H_2(v'')$ due to vibrational energy transfer between $Cs(v'') + H_2(v'')$;

$$Cs^* + H_2 \rightarrow Cs + H_2(X^1\Sigma_g^+) \rightarrow Cs + H^- + H. \tag{6.6}$$

On the other hand, the destruction process such as mutual neutralization,

$$H^- + \text{alkali}^+ \rightarrow H^0 + \text{alkali}, \tag{6.7}$$

is also important to clarify the total H^- production. In this paper some initial results, which are obtained from simultaneous observations of the H^- density, the work function of a plasma electrode and the alkali atom density, are reported by use of the photodetachment method, the photoelectron emission method, and the spectroscopic measurement in front of a plasma electrode. The correlation between the work function of the plasma electrode and the n_-/n_e ratio is observed by use of this direct measurement of negative ions in a volume source.

6.2 Experimental setup and method

A. Experimental setup

Figure 6.1 shows the illustration of the experimental setup for the photoelectron current, the photodetachment, and spectroscopic measurements. The 12 rows of Sm-Co magnets for plasma

confinement are attached to the surface of the cylindrical vessel (8.5 cm in diameter and 10 cm in length) made of copper. The end flange also has 4 rows of magnets for plasma confinement, two current feedthroughs, and a quartz glass window to pass through the intense laser light used for photodetachment without causing a reflection and stray light. Hydrogen plasma is generated by two cathode filaments (0.35 mm in diameter, 100 mm in length). The side wall is biased positively with respect to the cathode filaments to serve as the anode under dc mode operation. In the extraction region, where the details are shown in Fig. 6.2, the stainless steel vessel has three ports. Each port is used for a spectroscopic measurement, an electrical probe, and an alkali metal reservoir, respectively. The range of wavelength of the spectroscope (Hamamatsu, PMA-11, which has been improved to measure the spectrum in the near infrared region) is swept from 300 to 900 nm. The brightest line of alkali D lines can be detected. The cylindrical Langmuir probe located in front of the plasma electrode is made of a tungsten wire of 0.35 mm in diameter and its tip is 10 mm in length. Metallic Rb or Cs of 1 g is put into the alkali metal reservoir. Each temperature of the feedthrough pipe kept at 270 °C and the reservoir operated around 200 °C is controlled by use of a pair of heaters and thermocouples. The vapor pressures for rubidium and cesium at an oven temperature are calculated approximately in consideration of the oven design.(see Appendix B)

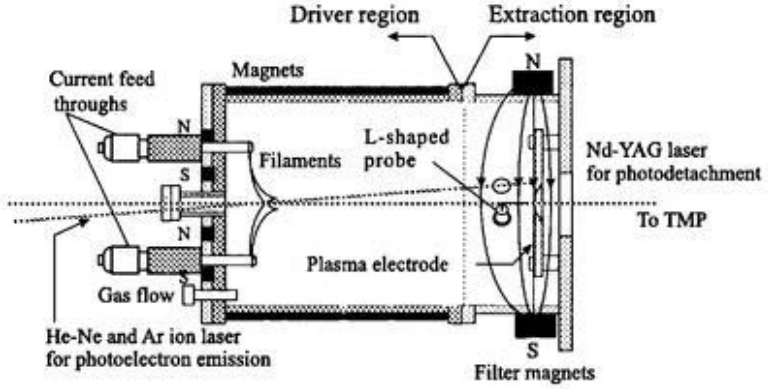

Figure 6.1: Illustrations of multicusp ion source and Langmuir probe. The alkali metal reservoir is not shown here.

B. Diagnostic systems

The laser photodetachment technique [2] is used to measure the n_-/n_e ratio. The work function of the molybdenum plasma electrode is measured by using the photoelectron emission

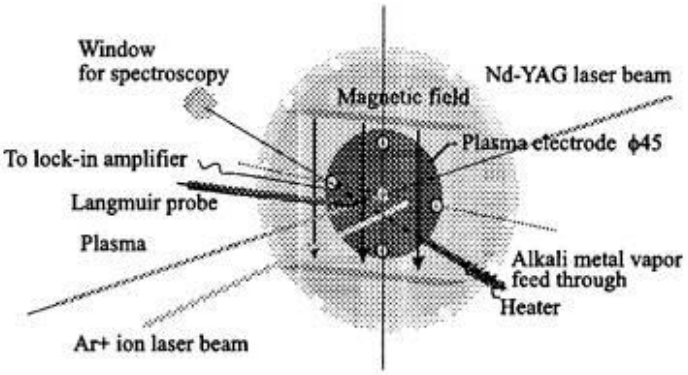

Figure 6.2: Displacement for the simultaneous measurements of work function and negative ion density in the extraction region of the ion source.

method [17]. We used an Ar^+ ion laser (Coherent, photon energy $h\nu$ = 2.41 eV, maximum output power W_L = 3 W) chopped at a frequency of 2 kHz, a He-Ne laser (NEC, $h\nu$ = 1.96 eV, W_L = 30 mW) chopped at a frequency of 1 kHz, and two lock-in amplifiers for the detection of photoelectron signals. Two chopped laser beams are mixed and introduced into the ion source. It is irradiated perpendicular to the plasma electrode biased at - 60 V. The reflected laser beam on its surface exits from the entrance window in order not to hit the other part of ion source.

C. Measurement of Negative Ion-Electron Ratio, n_-/n_e, by Photodetachment in Weak B Field

We used the photodetachment method assisted with a cylindrical Langmuir probe. Then the effect of the magnetic field in the extraction region must be taken into account. The magnetic field is 1.2 kGauss on the surface of magnet, and 100 Gauss at the probe position, which is perpendicular to the probe axis. T_e obtained from the probe $I-V$ characteristics is at most T_e = 1 eV. Meanwhile T_i is reported to be 0.5 eV at most. Under these conditions the Larmor radii of electrons ρ_e and ions ρ_i, are both the same order or larger than both the probe radius and the Debye length. Therefore we treat the measured electron current and the n_-/n_e ratio without any correction in the present condition.

6.3 Results

A. Simultaneous Measurements of n_-/n_e, Work Function and Spectral Lines

The emission spectra from the ion source plasma with Rb and Cs are shown in Fig. 6.4. These spectra are measured as the line integral in the radial direction in front of the plasma electrode.

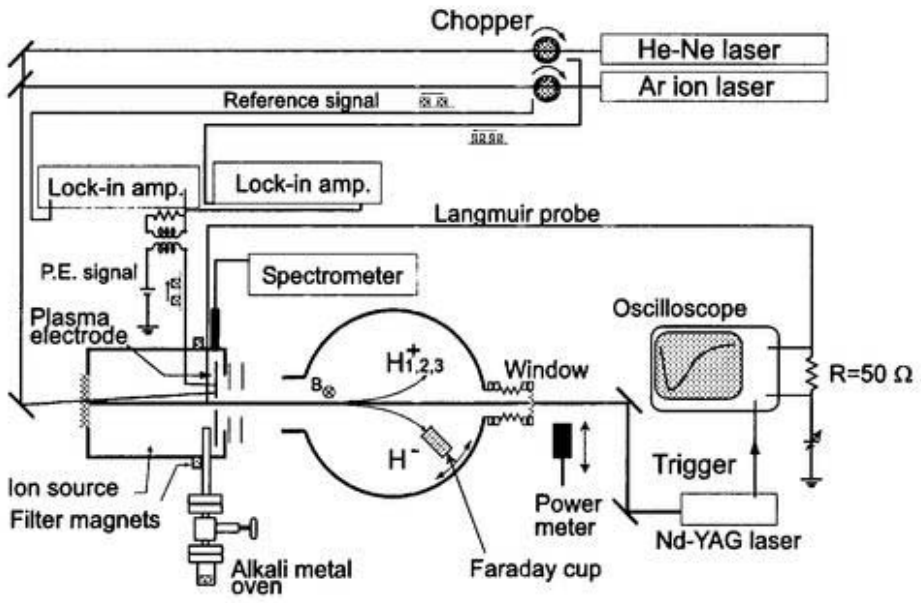

Figure 6.3: Displacement for the simultaneous measurements of work function and negative ion density in the extraction region of the ion source.

The light from the filaments lifts up the base line of spectrum. This is checked without the discharge. As the temperature of alkali metal reservoir is increased gradually around 180°C, Cs or Rb lines are emerged at 852.1 and 894.3 nm in Cs seeded case, and at 780 and 794.8 nm in Rb seeded case. Except for their bright lines, low intensities of RbII or CsII lines are also observed over the wide range. In view of the verification of Rb or Cs injection, the brightest line(780 nm for Rb, and 852.1 nm for Cs) are monitored. The unknown lines, which are similar to Cs D-lines in the infrared region, are always observed in Rb case. These lines would not be those of remained Cs in previous experiments, because inside the wall and the reservoir are washed by water and baked out by heater and filaments of the ion source. Thus the unknown lines would be optical emissions from Rb. Balmar lines of hydrogen H_α, H_β, H_γ, are observed in the H_2 discharge.

When Rb vapor begins to be introduced into the ion source in the H_2 discharge, firstly the n_-/n_e ratio increases gradually from 0.4 to 0.75, as shown in Fig. 6.5. At the same time, $I_{p.e.}$ increases suddenly at $I_{Rb} = 500$. $I_{p.e.}$ can not be detected when $I_{Rb} < 500$. This is the reason why the work function on the surface of plasma electrode is higher than the photon energy of Ar^+ ion laser 2.4 eV. Therefore the work function has been going down during no $I_{p.e.}$ signal. Closed symbols were measured three hours later after the valve of the rubidium reservoir was closed.

The variation with n_-/n_e ratio and work function is plotted against the intensity of rubidium spectral line, I_{Rb}, in Fig. 6.6. The values of the work function were calculated from those of measured photoelectron current using Eq. (2.18). Before the addition of Rb the n_-/n_e ratio was about 0.4 and the signal of photoelectron current was zero. The n_-/n_e ratio went up slowly with increasing the reservoir temperature. The n_-/n_e ratio became the maximum value and then the work function reduction reached the peak value. At this time the minimum work function of molybdenum surface adsorbed by rubidium becomes 1.8 eV at $I_{Rb} = 1200$. When I_{Rb} increased further, Φ reaches 2.1 eV. The plasma electrode would be covered with the thick rubidium, because Φ is close to the intrinsic work function of rubidium. We found the n_-/n_e ratio is sensitive to the change of the work function at the surface of the plasma electrode.

From this result, the surface production of H^- ions may be dominant in H_2 + alkali mixture plasma, since the n_-/n_e ratio reaches the maximum value at the work function minimum. As another possibility we can consider the change of the plasma potential due to the work function reduction causes the improvement of the plasma confinement in the driver region. If this is the case, the correlation between the work function and the plasma potential must be investigated.

B. Comparison between Cs and Rb adsorption

In case of cesium seeding, the maximum value of the n_-/n_e ratio agrees with the point of the minimum work function, while the difference in the H^- enhancement due to mass of Rb(M = 85.5) and Cs(M = 132.9) does not appear clearly in these experiments. In both Rb and Cs cases, as alkali D lines are larger than the H_α line, the n_-/n_e ratio decreases gradually, as shown in Figs. 6.6 and 6.7. This result may mean the mutual neutralization between H^- ions and positive ions of alkali atoms, or the collisional electron detachment with alkali atoms.

Figures 6.8 and 6.9 show the variations of n_- and n_e with discharge current for comparison between rubidium and cesium injection, while the enough alkali vapor was supplied into the ion source. The enhancement of n_-/n_e was observed in both cases. The work function of the surface would reach the intrinsic work functions of alkali metal due to thick alkali coverage. The differences between Rb and Cs were quite small, because the intrinsic work function for Rb is almost the same as that for Cs(see TABLE I).

C. Dependence of n_- and n_e on discharge current

When constant alkali metal vapor is introduced into the ion source, n_- and n_e in the extraction

region are measured in Figs. 6.8 and 6.9. In both cases, the difference in n_e is influenced by the magnetic filter field, and n_e and n_- have the same tendency due to the addition of alkali metal vapor. n_e is reduced to about one-half, while n_- increases from 1.1 to 1.7 times higher with the increase of I_d. The addition of alkali metal vapor is effective in the H^- enhancement at higher discharge current. V_s and T_e are also obtained. The plasma potential decreases clearly about 1 $\sim$ 2 eV, while the electron temperature does not change or decreases at most about 0.2 eV.

D. Dependence of n_-/n_e on electron temperature

We found that the work function of plasma electrode is correlated with n_-/n_e. Next, the components of H^- ions produced in the volume and on the surface are discussed. n_-/n_e ratios are plotted as a function of the electron temperature in Fig. 6.10. The electron temperature is controlled by the discharge current. n_-/n_e ratios in the extraction region are scattered, because slight misalignment of the probe causes the large ambiguity of n_-/n_e due to magnetic fields. At $T_e = 4.5$ eV, n_-/n_e becomes maximum regardless of with and without alkali metal vapor. When n_-/n_e corresponds approximately to the cross section for dissociative electron attachment of $H_2(v)$, $\overline{\sigma v}(DA)$, this peak at $T_e = 4.5$ eV agrees with $\overline{\sigma v}(DA)|_{v=8,9}$, calculated by Wadehara [1]. This result means that the volume production component of H^- ions is not influenced by alkali metal vapor.

6.4 Discussion

Possible reasons for enhancement of H^- ions are discussed in section 6.1. We consider which reasons are proper for H^- enhancement in the addition of alkali metal vapor. In a pure hydrogen discharge Bacal et al. and Fukumasa estimated plasma parameters numerically, using the rate equation in plasmas. Employing the same manners, we apply it to the results of Fig. 6.10. First, plasma without alkali metal vapor is treated.

Plasma parameters in the driver region would not be changed so much. This result has already been obtained in the previous chapter. Table 6.1 shows the reactions, which are discussed, and rate coefficients. These data are measured or estimated theoretically. The rate equation for negative ions is given by

$$\begin{aligned}\frac{dn_-}{dt} &= n(v^*)n_e\overline{\sigma v}(DA) + n_{H_2^+}n_e\alpha_2 + n_{H_2}n_e\alpha_3 \\ &\quad - n_{H^+}n_-\alpha_6 - n_{H_2^+}n_-\alpha_7 - n_{H_3^+}n_-\alpha_8\end{aligned}$$

Table 6.1: Reactions and rate coefficients

Reaction	Reaction rate	$(10^{-9}\mathrm{cm}^3\ \mathrm{s}^{-1})$
H^- Production		
$H_2 + e \rightarrow H_2(v'' = 8) + e_{slow}$	α_1	
$H_2(v'' = 8) + e_{slow} \rightarrow H^- + H$	$\overline{\sigma v}(DA)$	8.5
$H_2^+ + e \rightarrow H^- + H^+$	α_2	0.2
$H_2 + e \rightarrow H^- + H$	α_3	0.00006
Addition of alkali metal vapor		
$H, H^+ + e_{wall} \rightarrow H^-\ (+ H, H_2)$	$1/\tau_{ps}$	—
H^- Destructions		
$H^- + e \rightarrow H + 2e$	α_4	10
$H^- + e_f \rightarrow H + e_f + e$	α_5	—
$H^- + H^+ \rightarrow 2H$	α_6	500
$H^- + H_2^+ \rightarrow H + H_2$	α_7	100
$H^- + H_3^+ \rightarrow H_2(v) + H$	α_8	100
$H^- + H \rightarrow H_2 + e$	α_9	1.0
$H^- + H_2 \rightarrow H + H_2 + e$	α_{10}	0.494
$H^- + \mathrm{wall} \rightarrow H + e$	$1/\tau_{diff}$	
Other reactions		
$H_2^+(v) + H_2(v = 0) \rightarrow H_2^+(v) + 2e$		
$H_2^+(v) + e_{wall} \rightarrow H_2(v^*)$		
$H_3^+(v^*) + e_{wall} \rightarrow H_2(v^*) + H$		
$H_3^+(v^*) + H_2(v = 0) \rightarrow H_3^+(v < v^*) + H_2(v)$		
$e + H_2(X^1\Sigma_g^+, v = 0) \rightarrow e + H_2(B^1\Sigma_u^+, C^1\Pi_u, ...v')$		
$\rightarrow h\nu + H_2(X^1\Sigma_g^+, v') + e$		

$$- n_- n_e \alpha_4 - \frac{n_e}{\tau_{diff}}. \tag{6.8}$$

Many reactions and information of rate coefficients in plasmas make it difficult to understand the phenomena. Therefore several approximations are necessary for the analysis in plasmas, In particular, these reactions should not be applied to the extraction region because there do not exist high energy electrons due to the magnetic filter. The term of H^- loss reactions due to high energy electrons is removed. Since $n_2 n_e \alpha_2$, $N_2 n_e \alpha_3$, $n_- n_1 \alpha_6$, and $n_- N_1 \alpha_9$ are lower than those of the other reactions under the condition of $T_e = 1$ eV, these terms are neglected.

Now, as the plasma treated here is steady state, the left side hand of above equation is equal to zero. Thus Eq. (6.8) is transformed into

$$\frac{n_-}{n_e} = \frac{n(v^*)\overline{\sigma v}(DA)}{n_e \alpha_4 + n_{H^+}\alpha_6 + n_{H_2^+}\alpha_7 + n_{H_3^+}\alpha_8 + 1/\tau_{diff}}. \tag{6.9}$$

There exist only low energy electrons in the extraction region, but no high energy electrons, due to the magnetic filter. As $n(v^*), n_+, \overline{\sigma v}(ii), 1/\tau_{diff}$ would not depend on the low energy component of electrons, Eq. (6.9) is reduced to

$$\frac{n_-}{n_e} = \alpha \overline{\sigma v}(DA). \tag{6.10}$$

This means that n_-/n_e ratio corresponds to the cross sections for dissociative attachment of electrons, so that $\overline{\sigma v}(DA)|_{v=8,9}$ for vibrational states of $H_2(^2\Sigma_g^+, ^2\Sigma_u^+)$, which has the peak at $T_e = 0.3 \simeq 1$ eV, is chosen from their calculations of Wadehara [19]. Although the changes of I_d for acquiring the T_e dependence cause variations of n_e by a factor of 3 substantially, α keeps constant because of $n_e \alpha_4 \ll n_{H^+}\alpha_6 + n_{H_2^+}\alpha_7 + n_{H_3^+}\alpha_8 + 1/\tau_{diff}$. Substituting the values of table 6.1 into Eq. (6.9), one can obtain α for $T_e = 1$ eV in Eq. (6.10) and the curves for $v = 8$, and 9 in Fig. 6.10. The curves calculated agree with the measured data substantially.

On occasion that Cs is introduced into an ion source, it may be considered that H^- ions would be produced on a metal surface of low work function; H, $H^+ + e_{wall} \rightarrow H^-$. This assumption becomes one possibility and reasonable for H^- enhancement, because n_-/n_e is correlated with the work function of the plasma electrode. If the number of H^- created per unit time in unit volume is $1/\tau_{sp}$, Eq. (6.9) is transformed to

$$\frac{n_-}{n_e} = \frac{n(v^*)\overline{\sigma v}(DA) + [(n_H + n_{H^+})/n_e]\,1/\tau_{sp}}{n_e \alpha_4 + n_{H^+}\alpha_6 + n_{H_2^+}\alpha_7 + n_{H_3^+}\alpha_8 + 1/\tau_{diff}}. \tag{6.11}$$

For rough estimate, one may assume $n_{H^+} \ll n_H$ at the gas pressure of $P_g >$ a few mTorr, and

then one can neglect the term n_{H^+}.

$$\frac{n_-}{n_e} = \frac{n(v^*)\overline{\sigma v}(DA) + (n_H/n_e)1/\tau_{sp}}{n_e\alpha_4 + n_{H^+}\alpha_6 + n_{H_2^+}\alpha_7 + n_{H_3^+}\alpha_8 + 1/\tau_{diff}}. \quad (6.12)$$

$$= \alpha\overline{\sigma v}(DA) + \beta_{sp}. \quad (6.13)$$

From this equation, it is found that n_-/n_e ratios both with and without alkali metal vapor are laid to overlap each other. Broken curves in Fig. 6.10 are calculated under the conditions of $n_e = 5 \times 10^{10}$ cm^{-3} and $n_H = 10^{11}$ cm^{-3} [20]. As n_e goes down by a factor of 1/2 in the addition of alkali metal vapor, this value of the electron density would be reasonable. Unknown parameter $1/\tau_{sp}$ is estimated to be 2.38×10^3 s^{-1} by the optimum fitting. Since τ_{sp} is of the order of τ_{diff}, H^- ions are produced on the wall at the same rate of H^- loss, otherwise, H^- loss would be reduced on the wall. There is the way of the improvement for H^- loss on a surface.

The improvement of H^- density is seen at the higher discharge current, as shown in Figs. 6.8 and 6.9. The increase of H^+ ions would cause the increase of the surface production of H^- ions. H^+ inflow from the driver region would also cause the increase of surface production of H^- flow. In addition to these possibilities, the reduction of plasma potential in the extraction region may facilitate the H^+ flow from the driver region.

In the case that T_e is higher than 0.5 eV, the electron cooling can enhance the volume production of H^- ions. However this apparent electron cooling may have a possibility of the problem of the probe measurement in high n_-/n_e ratios. one must treat the probe $I - V$ characteristics carefully because the apparent electron temperature seems to be lower due to higher n_- current in the retarding region.

Figure 1.5 shows the potential energy curves for alkali hydrides and their negative ions. The potential energy curve for CsH^- is lower than that for H_2^-. H^- production at the surface is considered to be the dissociation from CsH^-. The vibrational states of CsH may cause the enhancement of the dissociative attachment of electrons to the molecules similar to the volume production of H^- ions.

We do not refer to a plasma response after photodetachment in magnetized plasmas. The limit of the Langmuir probe theory would require the confirmation between the different techniques for measurements of perturbed electron density, for example, microwave interferometer, laser interferometer, and Langmuir oscillation, etc. The measurements of vibrational molecules of H_2, hydrogen atoms, and molecular ions would be also required in the future.

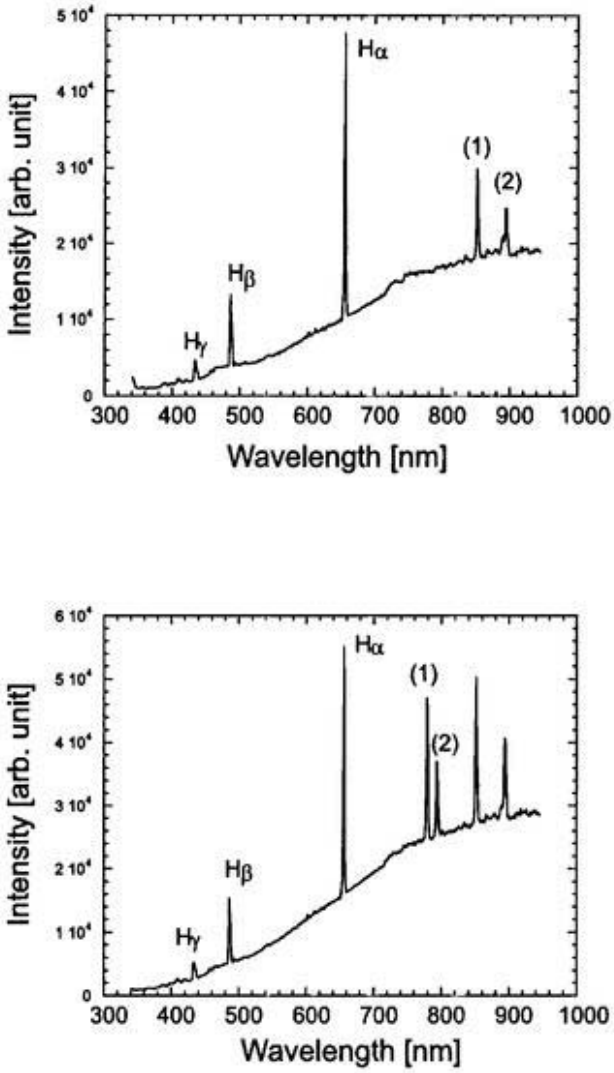

Figure 6.4: Optical emission spectrum of Cs(upper graph) and Rb(lower graph) in the extraction region in the H_2 discharge. V_d = 100 V, I_d = 4 A, P_g = 6.6 mTorr. In Cs case: (1)852.1nm, CsI($6s^2S_{1/2}$ - $6p^2P_{3/2}$), (2)894.3 nm, CsI($6s^2S_{1/2}$ - $6p^2P_{1/2}$). In Rb case: (1)780 nm, RbI($5p^2P_{3/2}$ - $5s^2S_{1/2}$), (2)794.8 nm, RbI($5p^2P_{1/2}$ - $5s^2S_{1/2}$).

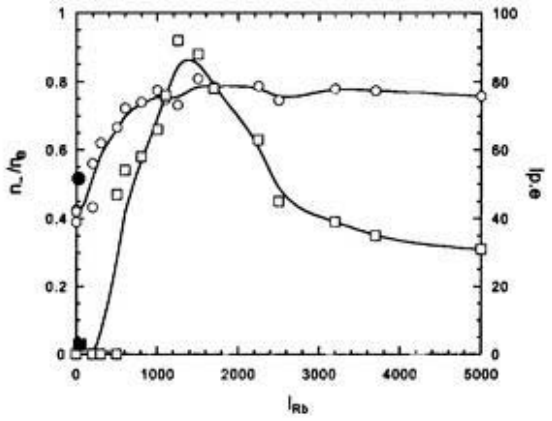

Figure 6.5: Variation of n_-/n_e and photoelectron current with the emission intensity of Rb in the extraction region in the H_2 discharge. $V_{pe} = -60$ V, $W_L = 104$ mW, and $f_{chop} = 1.14$ kHz.

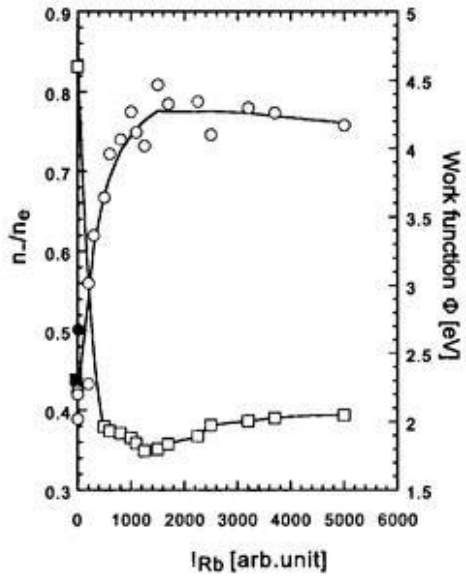

Figure 6.6: Vriation of n_-/n_e and work function with the emission intensity of Rb in the extraction region in the H_2 discharge. $V_{pe} = -60$ V, $W_L = 104$ mW, and $f_{chop} = 1.14$ kHz.

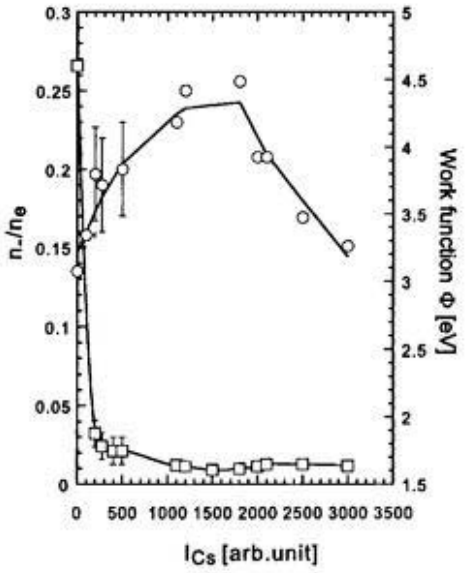

Figure 6.7: Variation of n_-/n_e and work function with the emission intensity of Cs in the extraction region in the H_2 discharge. $V_{pe} = -60$ V, $W_L = 104$ mW, and $f_{chop} = 1.14$ kHz.

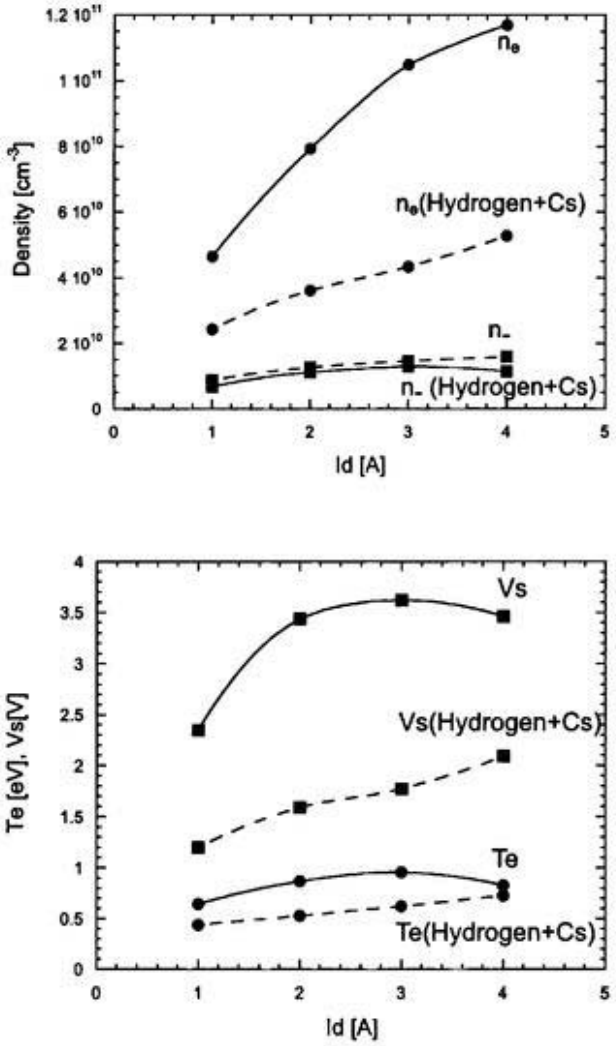

Figure 6.8: Dependence of n_e and n_- (upper graph) on the discharge current I_d for the cases of with(broken curve) and without Cs(solid curve). The lower graph is the dependence of T_e and V_s on the discharge current. The hydrogen gas pressure maintained constant P_g of 3.5 mTorr.

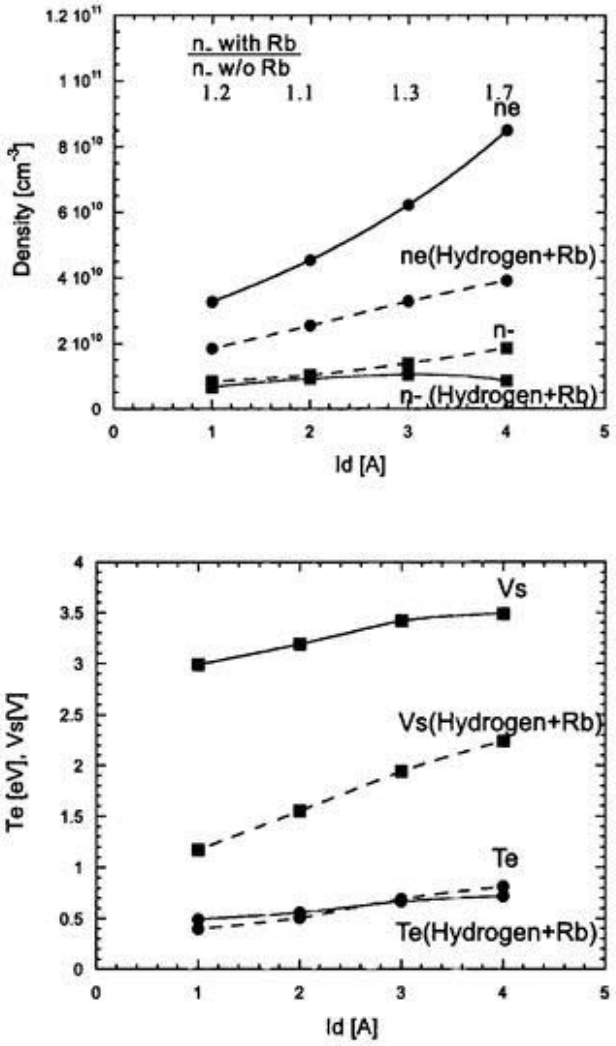

Figure 6.9: Dependence of n_e and n_- (upper graph) on the discharge current I_d for the cases of with(broken) and without Rb(solid). The lower graph is the dependence of T_e and V_s on the discharge current. The hydrogen gas pressure maintained constant P_g of 3.5 mTorr.

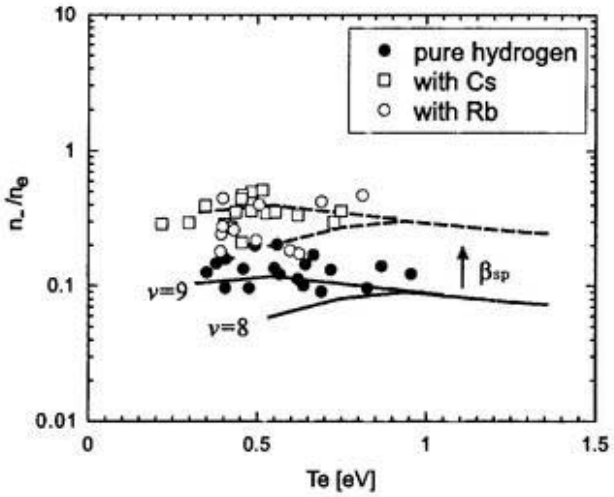

Figure 6.10: Variation of n_-/n_e with the electron temperature in the extraction region in the H_2 discharge. Closed circles are measured data in the pure hydrogen discharge. Open circles and squares in Rb and Cs seeded cases, respectively. Two solid curves indicate the cross sections for dissociative electron attachment of $H_2(v = 8, 9)$, $\overline{\sigma v}(DA)$, calculated by Wadehara [1]. Broken curves are calculated in consideration for the surface production of H^- ions. This is discussed in Sec. 6.4.

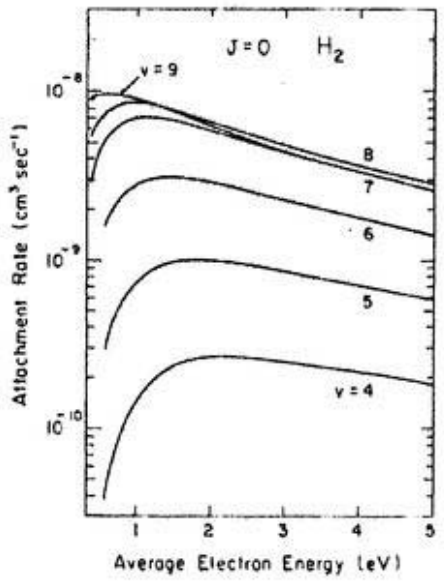

Figure 6.11: Dissociative attachment rate for various vibrational states($4 \leq v \leq 9$) of H_2 molecules($J = 0$), calculated by Wadehra [19]

Bibliography

[1] J. M. Wadehra and J. N. Bardsley, Phys. Rev. Lett. **41**, 1795(1978).

[2] M. Bacal, A. M. Bruneteau, W. G. Graham, G. W. Hamilton, and M. Nachman, J. Appl. Phys. **52**, 1247(1981).

[3] S. R. Walther, K. N. Leung, and W. B. Kunkel, J. Appl. Phys. **64**, 3424(1988).

[4] Y. Ohara, Rev. Sci. Instrum. **69**, 908(1998).

[5] K. Tsumori, A. Ando, Y. Takeiri, O. Kaneko, Y. Oka, T. Okuyama, H. Kojima, Y. Yamashita, T. Kawamoto, R. Akiyama, and T. Kuroda, Rev. Sci. Instrum. **65**, 1195(1994).

[6] P. J. Schineider, K. H. Berkner, W. G. Graham, R.V. Pyle, and J. W. Stearns, Phys. Rev., B**23**, 941(1981).

[7] J. N. M. Van Wunnick, J. J. C. Geerlings, E. H. A. Granneman, and J. Los, Surf. Sci. **131**, 17(1983).

[8] K. N. Leung, C. F. A. Van Os, and W. B. Kunkel, Appl. Phys. Lett. **58**, 1476(1991).

[9] W. G. Graham, Phys. Lett., 73A, 186(1979).

[10] S. T. Melynychuk, M. Seidl, W. Carr, J. Isenberg, and J. Lopes, J. Vac. Sci. Technol. A**7**, 2127(1989).

[11] T. Okuyama and Y. Mori, Rev. Sci. Instrum. **63**, 2711(1992).

[12] K. Shinto, Y. Okumura, T. Ando, M. Wada, H. Tsuda, T. Inoue, K. Miya-moto and A. Nagase, Jpn. J. Appl. Phys. **35**, 1894(1996).

[13] O. Fukumasa and E. Niitani, Jpn. J. Appl. Phys., Part2 **35**, 1528(1996).

[14] M. Bacal, F. El Balghiti-Sube, L. I. Elizarov and A. Y. Tontegode, Rev. Sci. Instrum. **69**, 932(1998).

[15] W. J. Stevens, A. M. Karo, and J. R. Hiskes, J. Chem. Phys. **74**, 3989(1981).

[16] J. R. Peterson, 4th International Symposium on the Production and Neutralization of Negative Ions and Beams, Brookhaven, 1986, AIP Conf. Proc. No. 158, pp. 113-117.

[17] Y. Okabe, M. Sasao, H. Yamaoka, M. Wada and J. Fujita, Jpn. J. of Appl. Phys. **30**, 1307(1991).

[18] G. D. Alton, Nucl. Instrum. Method., B**37/38**, 45(1989).

[19] J. M. Wadehra, Appl. Phys. Lett. **35**, 917(1980).

[20] O. Fukumasa, J. Phys. D: Appl. Phys. **22**, 1668(1989).

[21] K. W. Ehlers and K. N. Leung, Rev. Sci. Instrum. **53**, 1423(1982).

Chapter 7

Conclusions

The laser photodetachment technique in plasmas with negative ions has been studied experimentally and theoretically throughout this thesis, and applied to the diagnostics of ion sources.

The different photon energies of a Nd-YAG laser have been used to investigate the influence on the photodetachment current captured by a Langmuir probe for the determination of the H^- density and the H^- drift velocity. From $\delta I_p - V_p$ characteristics, the photodetachment current is independent of the laser photon energies. Therefore the photon energies do not affect the determination of the H^- density, n_-, and the H^- temperature, T_-, obtained from the H^- drift velocity under the conditions of low n_-/n_e ratio(<1%). From the time variation of photodetachment current, the photon energies is independent of not only the H^- drift velocity v_{drift}, but also the ballistic velocity v_b. The H^- drift velocity is very close to the ion acoustic velocity of H_3^+ ions.

Using the Friedland's calculations with the hybrid fluid-kinetic model, we found that the positive ion temperature T_+ can be determined from the ratio of the overshoot and photodetachment current, $I_{ov}/\Delta I$. This ratio is not also affected by the photon energy.

The hybrid fluid-kinetic model is extended for the analysis of perturbed plasmas in time and space after photodetachment. Under the conditions of the collisionless, unmagnetized and low n_-/n_e ratio, this model for plasma responses with three species(H_3^+, electron, and H^-) is applied and compared with the experimental data inside($r \leq R$) and outside($r > R$) the laser beam in a cylindrical geometry.

At $r \leq R$, the time evolution of the calculated photodetachment signal reproduces well that of the measured signal. The ratio of the overshoot current to the perturbed current strongly

depends on T_+/T_e ratio, and hence the positive ion temperature can be obtained from this ratio in the limit $T_+ \ll T_e$. At $r > R$, the change of the calculated photodetachment current in time and space almost agrees with the observed current. Since the outward flow of electrons are related significantly with the dynamics of positive ions and negative ions, the negative ion density can be obtained strictly by the measurement at $r > R$ with the method shown in the present work.

In case of $n_-/n_e > 1$, the application of this model becomes difficult to determine the negative ion density, because the perturbed potential $\delta\phi$ affects the profile of its own potential. We can avoid the problem by a lowering of photodetachment rate, that is, the laser power is reduced down to $\delta n_e/n_e < 1$. As a different way, Ivanov et al. have extended the kinetic theory of a plasma response developed by Landau, and O'Neil et al. in a plane geometry. One can use the theory in a proper geometry under the conditions of high n_-/n_e ratio.

The laser photodetachment technique is applied to actual ion sources in order to understand the enhancement of H^- density due to the addition of cesium vapor. Then the amount of cesium vapor in the ion source is monitored spectroscopically. In the driver region, it is found that the drastic changes in plasma parameters are not observed except for the increase of the plasma space potential.

We have carried out the similar experiment in the extraction region, because the extracted H^- beam is considered to be correlated significantly with the conditions of the extraction region, especially the work function of the plasma electrode. The work function on the surface of the plasma electrode is obtained by the measurement of the photoelectric current generated by the Ar^+ ion laser. The intensity of the cesium D line increases with the increase of the oven temperature, and the n_-/n_e ratio goes up immediately by a factor of 2. The yield maxima of H^- density correlate closely with the work function minima. When more cesium vapor is introduced into the source, the work function reaches the intrinsic work function of cesium. At that time the H^- density saturates, or gradually decreases. The similar results are obtained in the case of Rb. We find out that the H^- density in the extraction region is strongly correlated with the work function of the plasma electrode.

In order to explain the enhancement of n_-/n_e, we employed rate equations with the use of measured parameters. Then the measured correlation of H^- density with the work function minima allows us to assume the surface production of H^- ions. From the comparison between

the experimental results and the calculations, it is found that the surface production of H^- ions is reasonable for the explanation of the enhancement of n_-/n_e in the cesium seeded case. For the sake of more efficient production of negative ions in an volume source, the low work function surface in the extraction region is one of the most essential elements.

From these results, this study is summarized as follows;
The laser photodetachment technique has been verified in consideration with the plasma response, and then

- The plasma parameters obtained are not influenced by the laser wavelengths(photon energies).
- From the comparison between experiments and calculations, it is found that the hybrid fluid-kinetic model represents the plasma responses induced by laser photodetachment well. The physical picture of plasma responses in photodetachment becomes clear.
- The negative ion densities and temperatures and the positive ion temperatures can be obtained.
- From the measurements not only inside, but also outside the laser channel, negative ion densities are determined.

From the application of the laser photodetachment technique to the actual ion sources,

- In the driver region, the enhancement of negative ion densities due to alkali metal seeding is not observed.
- In the extraction region, it is clear that the negative ion density is correlated with the work function of the plasma electrode.

Acknowledgments

I wish to express special thanks to Dr. M. Sasao of National Institute for Fusion Science(NIFS) and Dr. M. Bacal of Ecole Polytechnique, whose thoughtful supervision provided continuing guidance for this work. I thank Dr. M. Fujiwara of NIFS and Dr. T. Kuroda of Chubu University to give me the opportunity of the international collaboration researches at NIFS. I am also indebted to Dr. M. Wada and Dr. T. Kasuya of Doshisha University for their encouragement and discussion throughout this work. I would like to thank Mr. R. Ogiso and the technicians of NIFS for engineering and technical services of instruments for these experiments.

I acknowledge the encouragement given by Dr. M. Isobe, Dr. S. Inagaki, Dr. K. Tsuzuki, Dr. M. Hamabe, Dr. K. Hosasa, Dr. T. Takahashi, K. Ikeda, T. Imai, J. Chen, T. Kenmotsu, Y. Hasegawa, T. Kobuchi, T. Kondo, K. Matsushita, and H. Sasao, and also the members of LABCOM, diagnostic, and R&D group at NIFS.

I am grateful for desk works managed by the official staff; Mr. T. Kondo and Mrs. S. Koide, who are in charge of The Grad. Univ. for Adv. Studies at NIFS.

I must give immense thanks to my parents and my wife Etsuko. Their support during the doctoral course was of immeasurable value to me.

I would like to appreciate financial supports of the Japan Foundation Scholarship, Kakuyugo scholarship, and support of Inoue Foundation for Science on the occasion of the participation in 7th International Conference on Ion Sources(ICIS) in Italy.

Appendix A

Monopolar transport in negative-ion plasma

This appendix is mentioned for the ballistic theory, which is noted in section 2.2 of chapter 2 and in chapter 4.

Plasma dynamics after photodetachment in a negative containing plasma were first investigated by Stern et al..[1] The details are written in their paper. Other work by Skinner et al.[2] would be helpful in understanding the ballistic theory. One finds the need for studying a plasma response, especially that of perturbed electrons, using the hybrid fluid kinetic theory. From both of Stern et al. and Skinner et al. their approach is to evaluate only the ballistic term and neglects the field dependent term in an early time period.

The density and velocity distribution of negative ions at $t' = 0$ is used for the calculation of $n_B(r,t)$.

$$n_B \equiv \int d\mathbf{v} \left[f\left(\mathbf{v}, \mathbf{r}', t'\right) \right] |_{t'=0}. \tag{A.1}$$

The solution of perturbed negative ions has the following form;

$$\frac{n_B(r,t)}{n_0} \equiv J\left(\left(R_{min}/v_{th}t\right)^2, \left(r/v_{th}t\right)^2 \right) - J\left(\left(R_{max}/v_{th}t\right)^2, \left(r/v_{th}t\right)^2 \right). \tag{A.2}$$

$$J(x,y) \equiv 1 - 2e^{-\rho^2} \int_0^\beta te^{-t^2} I_0(2\rho t)\, dt,$$
$$x = \beta^2, y = \rho^2,$$

where R_{min} is the laser radius, and R_{max} is the source radius. When $r = 0$, $n_{-B}(0,t)$ becomes

$$\frac{n_{-B}(0,t)}{n_{-0}} \simeq J\left(\left(R/v_{th-}t\right)^2, 0 \right) = e^{-\left(R/v_{th-}t\right)^2}. \tag{A.3}$$

[1] Ref. [5] in chapter 3
[2] Ref. [9] in chapter 4

This equation represents the time evolution of negative ion density at $r = 0$, as is shown in Fig. A.1. Equation (A.3) corresponds to Eq. (4.15) at $r = 0$.

From Eq. (A.3), we introduce Eq. (2.12) easily. When the time t_1 defines $1/e$ recovery time of H^- ions at $r = 0$ after photodetachment, the power of the right hand side of Eq. (A.3) is equal to -1;

$$v_{th}^{-} = R/t. \tag{A.4}$$

When the correction of the probe radius must be carried out strictly, Eq. (A.3) is obtained. In r¿R case, the function J in Eq. (A.2) are dominated by the factor $r/v_{th-}t$, and thus Eq. (A.2) leads to Eq. (2.13).

In practice, Stern et al. detect this recovery curve using the double laser pulse photodetachment technique. There is a problem that the measured data is in disagreement with the ballistic theory in the longer time interval of second laser shot. They conclude the discrepancy is due to collisions and the higher-order potential effects. In addition to these reasons, Skinner et al. point out the shift of the effective collection area of the probe influences on the disagreement of theory with the experimental data.

The potential due to photodetachment propagates in a plasma. Poisson's equation is used to represent the phenomena. The density terms for electrons, negative, and positive ions in its equation are applied to the linearized Boltzmann's relation, the ballistic theory, and the quasi-neutrality, respectively.

$$\begin{aligned} \Delta^2\phi &= 4\pi e\left(n_e + n_- - n_+\right) \\ &= 4\pi e\left(n_{e0} + \delta n_e + n_- - n_{+0}\right). \end{aligned} \tag{A.5}$$

Using the following relations;$n_{+0} = n_{e0} + n_{-0}$, and $n_- = n_{-0} J\left((R/v_{th}t)^2, (r/v_{th}t)^2\right)$, Eq. (A.5) is transformed into

$$\begin{aligned} \Delta^2\phi &= 4\pi e\left(n_{e0}\left(\frac{e\Delta\phi}{\kappa T_e}\right) + n_- - n_{-0}\right) \\ &= 4\pi e\left(n_{e0}\left(\frac{e\Delta\phi}{\kappa T_e}\right) - n_{-0}\left(1 - J\left((R/v_{th}t)^2, (r/v_{th}t)^2\right)\right)\right). \end{aligned} \tag{A.6}$$

It assumes that the term $\Delta^2\phi$ would be negligible under the quasi-neutral condition. The right hand side of Eq. (A.6) becomes,

$$e\Delta\phi(r,t) = \frac{n_{-0}}{n_{e0}}\kappa T_e\left(1 - J\left((R/v_{th}t)^2, (r/v_{th}t)^2\right)\right). \tag{A.7}$$

The calculations of Eq. (A.7) are carried out in Fig. A.2 and A.3. The ballistic approach for the change of $\Delta\phi$ is indistinct apparently. The ballistic theory can not describe the potential propagation outward enough.

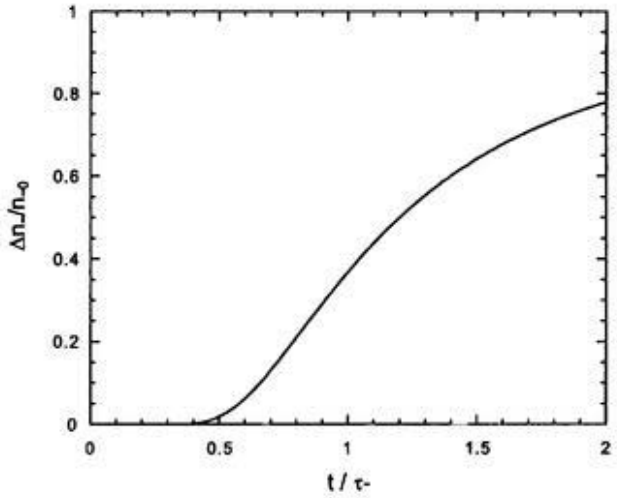

Figure A.1: Recovery of H^- density at $r = 0$ using the ballistic theory of Eq. (A.3).

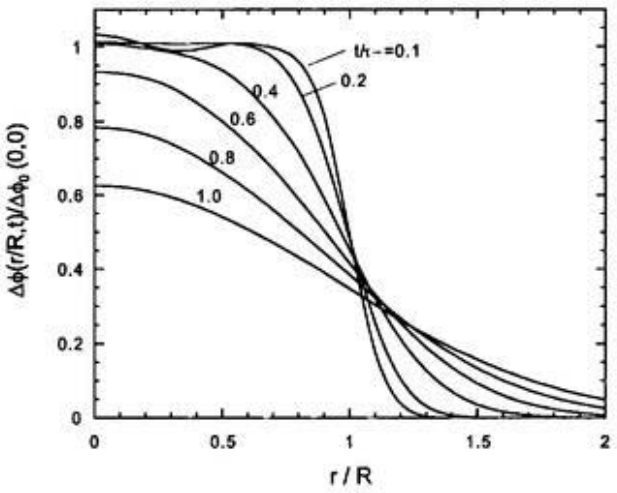

Figure A.2: Spatial distributions of the perturbed potential for various values of time normalized by the recovery time of H^-.

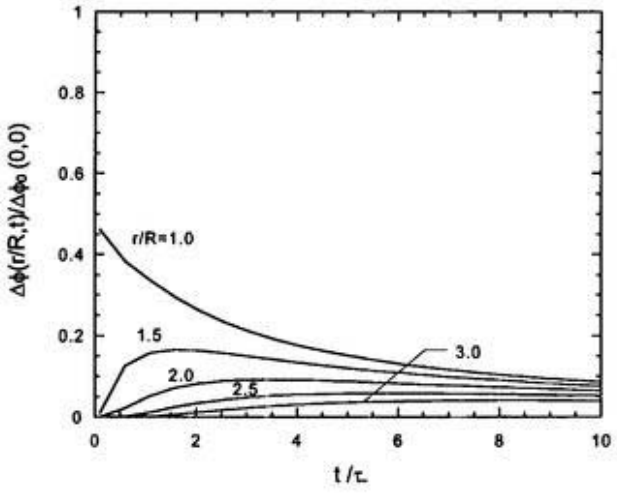

Figure A.3: Time evolution of the perturbed potential for various values of the probe position.

Appendix B

Estimate of cesium vapor pressure in an ion source

An alkali metal oven has been used in the experiment of chapter 6. We evaluate the vapor pressure for rubidium and cesium in the ion source at an operation temperature of the oven.

Cesium vapor is introduced into an ion source, when the alkali metal oven is heated up from a room temperature to 300 °C. The vapor pressure is governed by the conductance of the oven, which is determined by the construction of the cesium oven and the nozzle following to the ion source. Gas pressures of the ion source P_g and the oven P_{oven} are related with each other by

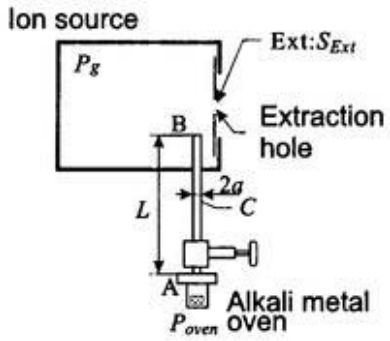

Figure B.1: Simplified illustration of an ion source with an alkali metal oven. S_{Ext} : cross section of the extraction hole, a : radius of the nozzle pipe, and L : length of the pipe. P_g and P_{oven} are gas pressures of the ion source and the oven, respectively.

the conductance of the nozzle pipe, C. In Rb or Cs seeding case, we may assume the valve has almost the same conductance as the nozzle pipe, because the valve is full-opened at that time. When ΔP is the difference of gas pressure between the point A and B, the flux from the point A

to B, $Q_{A\to B}$, with the mean velocity, $\overline{v}$, is given by

$$\begin{aligned} Q_{A\to B} &= C\Delta P & \text{(B.1)} \\ &= \frac{1}{4}\overline{v}\left(\frac{8\pi}{3}\frac{a^3}{L}\right)(P_{oven}-P_g), & \text{(B.2)} \end{aligned}$$

where a is radius of the nozzle pipe, and L length of the pipe. This flux $Q_{A\to B}$ is equivalent to the flux from the ion source to the extraction hole, so that

$$Q_{A\to B} = \frac{1}{4}\overline{v}S_{Ext}p_{BExt}P_g \qquad \text{(B.3)}$$

with the probability for passing through from the point A to B, p_{BExt}. From Eq. (B.2) and Eq. (B.3), the gas pressure of the ion source becomes;[1]

$$P_g = \frac{P_{oven}}{1+\frac{3}{8\pi}\frac{LS_{Ext}}{a^3}}. \qquad \text{(B.4)}$$

The vapor pressure for cesium P_{Cs}, at a temperature, T, is given by [2]

$$\begin{aligned} \log P_{Cs} &= \log P_{oven} \\ &= 7.256 - \frac{3753}{T}. & \text{(B.5)} \end{aligned}$$

In the case of the determination of the fitting equation for rubidium vapor pressure, we can obtain the fitting equation for data measured in Ref. [2], which is similar to the above equation:

$$\log P_{Rb} = 9.5763 - \frac{5434.3}{T}. \qquad \text{(B.6)}$$

Substituting the following values $L = 200$ mm, $a = 1.5$ mm, $A = 3^2\pi$ mm^2, into Eq. (B.4), P_g is represented as follows;

$$P_g = \frac{P_{oven}}{201}. \qquad \text{(B.7)}$$

Figure B.2 shows the dependence of the cesium vapor pressure on the oven temperature. Since T_{oven} changes in the range from 300 to 450 K, we can estimate the cesium gas pressure in the ion source to be the range from 10^{-6} to 10^{-1} Torr. In the case of Rb, the vapor pressure of Rb is lower than that of Cs at the same temperature. Therefore, higher oven temperature($300 \sim 480$ K) is required for the Rb case.

[1] J. Ishikawa, "Iongen Kogaku" in Japanese, (Ionix, 1985) Eq. (3-11) in page 87.
[2] A. N. Nesmeyanov, "Vapor Pressure of the Chemical Elements", (Amsterdam, Elsevier) p.144-150(1963)

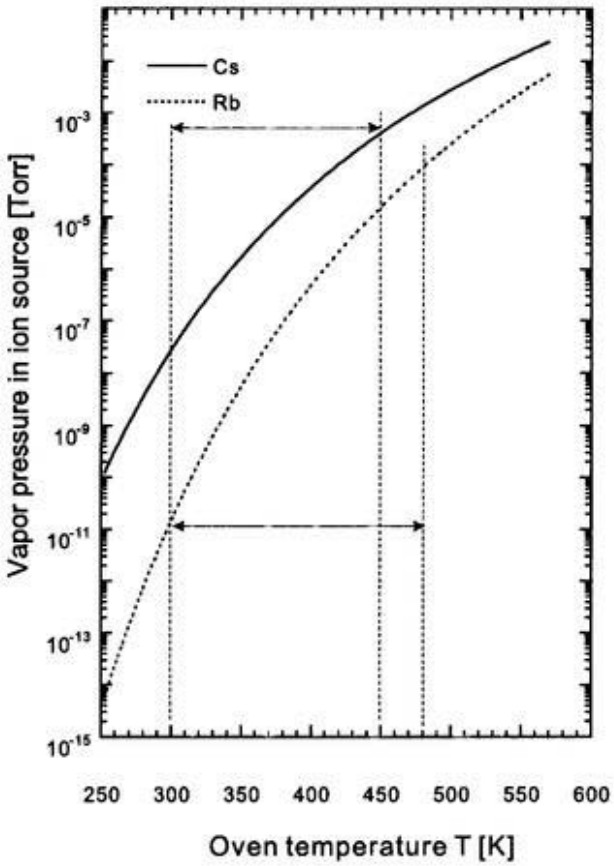

Figure B.2: Estimate of rubidium and cesium vapor pressures in the ion source. The arrows indicate the operation temperature of the oven for Rb and Cs, respectively.